Scaling and exceedance probability of sinkhole collapse in evaporite karst (Dead Sea, Jordan)

Hanna Z. Schulten[1,★], **Robert A. Watson**[1,★], **Djamil Al-Halbouni**[2], **and Eoghan P. Holohan**[1,3]

[1]UCD School of Earth Sciences, University College Dublin, Dublin, Ireland
[2]Institute for Earth System Science and Remote Sensing, Leipzig University, Leipzig, Germany
[3]iCRAG – Research Ireland Centre for Applied Geosciences, University College Dublin, Dublin, Ireland
★These authors contributed equally to this work.

Correspondence: Eoghan P. Holohan (eoghan.holohan@ucd.ie)

Received: 24 October 2025 – Discussion started: 25 November 2025
Revised: 19 August 2026 – Accepted: 11 September 2026 – Published:

Abstract. Quantitative analysis of sinkhole collapse hazard requires robust data in both space and time. It also needs a clear understanding of the factors and processes that contribute to observed sinkhole locations and dimensions. In many karst settings, these criteria are difficult to meet because of the millennia-long time scales over which sinkhole populations are generated and because of uncertainties around how geomorphological processes link to sinkhole dimensions. This study presents new data on the scaling and probability of sinkhole formation in evaporite karst on the eastern Dead Sea shore (Jordan). Several thousand cover collapse sinkholes have formed there in the past 40 years with minimal post-collapse modification. Genetic processes and timescales are thus well constrained. Utilising high-resolution satellite imagery (Pleiades, PNEO) from 2017–2024, integrated with prior datasets, we present an updated inventory of sinkhole occurrence, extent and dimensions through time over the period 1992–2024. The sinkhole number increased by 43 % from 1565 in 2018 to 2247 in 2024, reflecting a 22 % increase in the sinkhole-affected land area to ca. 179 610 m^2 (17.9 ha). Formation of new karst subsidence features has continued a northward and seaward advance, consistent with control from the decline of the Dead Sea base level. However, we also observed a localised revival in 2021–2022 of sinkhole formation in an area that had been apparently inactive since 2002. This combination of continued and renewed sinkhole formation poses significant challenges to agriculture, housing and infrastructure in the area. Sinkhole average diameters range from 0.8 TS1 to 72.9 m; their frequency follows a log-normal distribution, rather than a power-law. Representative annualised exceedance probabilities for formation of sinkholes with diameters greater than 5, 10 and 50 m are ca. 70 %, 30 % and 0.5 % respectively. Exceedance probabilities show slight dependence on sampling time interval and on the nature of near-surface materials in which sinkholes form. Given their log-normal size distribution, the Dead Sea cover collapse sinkholes are not scale-free; instead they are scale-bound by the evaporite karst system's geometrical and mechanical properties.

1 Introduction

The formation of collapse sinkholes is a widespread geohazard on Earth. Sinkhole collapses are in general related to groundwater movements that drive sub-surface physical and/or chemical erosion (karstification) of rocks made of water-soluble minerals (i.e., containing ions of carbonate, sulphate or chloride) (De Waele et al., 2011; Gutiérrez, 2016; Gutiérrez et al., 2014). While such processes can occur naturally, they can also be induced or amplified by anthropogenic activities. An important factor in the hazards posed by sinkhole formation is that the dissolution kinetics of the chloride and sulphate minerals (e.g. halite, gypsum and anhydrite) typical of evaporite karst environments are much faster than those of the carbonate minerals (e.g. calcite, dolomite) that usually make up the globally more widespread limestone karst environments. Evaporite karstification and related subsidence hazards can thereby develop much more rapidly than

Proof only

the case for carbonate karstification. Damaging and costly subsidence events related to evaporite dissolution have been documented around the world, for example in Great Britain (Cooper, 2002), Germany (Wadas et al., 2017), Spain (Galve et al., 2009), Kuwait (Shaqour, 1994), the United States (Johnson, 2008), and China (Yaoru et al., 2002).

A striking example of hazards posed by evaporite karstification is the ongoing generation of thousands of sinkholes around the Dead Sea (Fig. 1) (Abelson et al., 2017; Sevil and Gutiérrez, 2024; Taqieddin et al., 2000; Watson et al., 2019; Yechieli et al., 2006). The development of these sinkholes and other associated land subsidence phenomena over the past ∼ 40 years has led directly to the damage or destruction of houses, road infrastructure, tourism facilities, agricultural land, industrial buildings and other related structures (e.g. walls of evaporation ponds for potash production). The underlying cause is karstification of subsurface evaporite deposits rich in halite (rock salt), which is in turn caused by groundwater level changes associated with a largely anthropogenically-driven fall of the Dead Sea level by over 40 m since 1970 (Abelson et al., 2017; Al-Halbouni et al., 2017; Arkin and Gilat, 2000; El-Isa et al., 1995; Taqieddin et al., 2000; Watson et al., 2019; Yechieli et al., 2006).

Sinkholes at the Dead Sea occur on its western and eastern shores (Fig. 1b). The sinkhole population of the western shore is larger and more widespread; it comprises about 10 spatially distinct localities along a ca. 60 km stretch of coastline (Abelson et al., 2017). By mid-2015, the western shore localities collectively contained around 5500 holes (Abelson et al., 2017). The present sinkhole population size there is unclear, but the annualised rate of sinkhole formation in 2015 was about 400–700 holes yr^{-1} TS2 (Al-Halbouni et al., 2017; Nof et al., 2019). The sinkhole population on the eastern shore is almost entirely found at one locality – a 7 km long coastal strip to the north and west of the village of Ghor Al-Haditha in Jordan. By mid-2017, the eastern shore had about 1550 holes (Watson et al., 2019), i.e. ca. 20 % of the total of 7500–8000 sinkholes around the Dead Sea at that time.

As for other geohazards (e.g. landslides, earthquakes), characterisation of the size distribution (frequency-magnitude) of an existing sinkhole population could enable probabilistic forecasting of likely dimensions of newly formed sinkholes (Galve et al., 2008; Gökkaya et al., 2021; Sevil and Gutiérrez, 2024; Taheri et al., 2015). Furthermore, if timings of past sinkhole formation are well constrained, then such forecasts can be formulated in terms of annualised exceedance probabilities – i.e., the likelihood of formation of a sinkhole that exceeds a certain size in any given year. Sinkhole (or doline) size distributions in various karst settings (carbonate, sulphate, halite) outside of the Dead Sea have been previously modelled by using either power-law (Galve et al., 2011; Pardo-Igúzquiza et al., 2020) or log-normal functions (eg. Gökkaya et al., 2021; Gutiérrez et al., 2019; Sevil and Gutiérrez, 2024; Taheri et al., 2015; Verbovšek and Gabor, 2019). Both power-law and

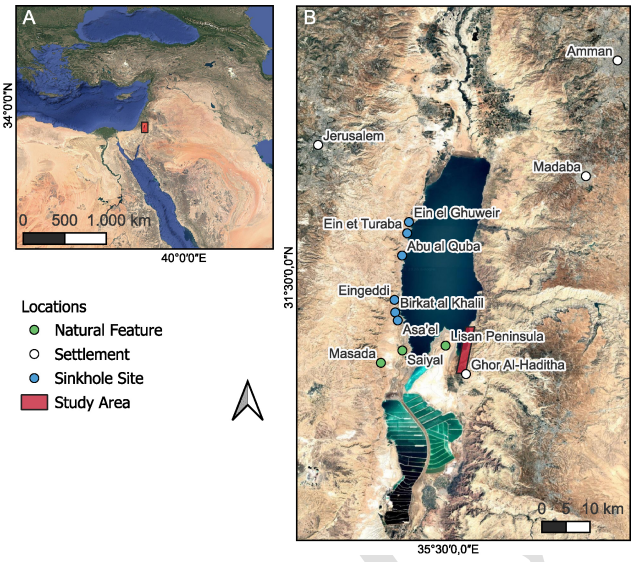


Figure 1. Location of the Ghor Al-Haditha study area. **(A)** Overview of the Middle East with location of the Dead Sea highlighted. **(B)** Overview of the Dead Sea region with location of Ghor Al-Haditha study area highlighted to the southeast of the northern Dead Sea sub-basin. Locations of previous TS3 sinkhole formation on the western Dead Sea shore are also marked. Base map: © Google Earth 2025; underlying data are from SIO, NOAA, U.S. Navy NGA and GEBCO and imagery is from Landsat and Copernicus.

log-normal distributions are highly skewed, such that the probability of formation of smaller holes is much higher than that of larger holes. A true power-law, however, is associated with scale invariance (scale-free behaviour) and a distribution in which the frequency of smaller holes increases progressively with decreasing hole size. A log-normal distribution, on the other hand, is associated with a lack of scale invariance (scale-bound behaviour) and a distribution in which the frequency of smaller holes diminishes below a certain size ("rollover") (cf. Stark and Hovius, 2001).

In practice, there are several issues in assessing the representativeness of such model distributions. Firstly, the spatial resolution of mapping may be insufficient to fully characterise the true population size distribution (cf. Stark and Hovius, 2001). Secondly, the relationship of size distribution to process(es) of depression formation, such as surface solution, suffusion, collapse or some combination (cf. Gökkaya et al., 2021), can be unclear if sinkholes form over many millennia. Thirdly, if ages of the depressions are poorly constrained, then: (i) post-formation modifications to depression geometry (e.g. by mechanical weathering and erosion) are largely unaccounted for; and (ii) time-linked probabilities are difficult or impossible to attain.

The Dead Sea region is perhaps uniquely suitable for a probabilistic approach to sinkhole hazard analysis. The highly arid environment means that, outside of relatively

Proof Only

small areas of farmland, there is minimal post-collapse modification of sinkholes via surface erosion or infilling. The process of sinkhole formation is strictly by collapse – mainly cover collapse with some limited bedrock collapse (cf. classifications of Gutiérrez et al., 2008). Unlike at the more slowly developed sulphate and carbonate karst terrains or at other evaporite karst settings in more humid environments (e.g., Gökkaya et al., 2021; Pardo-Igúzquiza et al., 2020), the Dead Sea sinkhole size/frequency relationship is minimally affected by non-collapse-related geomorphic processes.TS4 The timing of sinkhole formation in this largely unvegetated area is well constrained by ground surveys and multitemporal remote sensing observations, which allows for annual or multiannual probabilities. Lastly, the large number of holes and the high resolution of mapping yield a high data completeness and a statistically robust analysis.

Although some recent studies have capitalised on these attributes of the Dead Sea area to propose scaling laws for sinkhole sizes (Corral and González, 2019; Yizhaq et al., 2017) and temporal exceedance probabilities for sinkhole formation (Sevil and Gutiérrez, 2024), those studies focussed exclusively on the western Dead Sea shore. Moreover, the sinkhole size distributions there have been fit with have differing preferred scaling relationships: either power-law and thus scale-free (Yizhaq et al., 2017) or truncated log-normal and thus scale-bound (Corral and González, 2019; Sevil and Gutiérrez, 2024). Finally, it is unclear from these previous works how materials (alluvial vs lacustrine sediments) in which sinkholes form influence the size distributions.

In this paper, we present a first quantitative hazard assessment for sinkhole formation due to evaporite karstification on the eastern shore of the Dead Sea. We update the previously assembled inventory of sinkholes from that assembled previouslyTS5 for the period 1968–2017 (Watson et al., 2019) by analysing high resolution optical imagery from Pleiades A/B and Pleiades Neo satellites for the years 2018–2024 inclusive. In addition, we digitised polygons of sinkhole perimeters for the entire period of 1992–2024 to quantify the total land area affected by karst-related subsidence on the eastern shore through time. We analyse the scaling of sinkholes in the new datasets to provide exceedance probabilities for the annual rate of formation of sinkholes of given sizes. We consider the nature of the three main near-surface materials in which sinkholes form (alluvium, mud and rock salt) and whether sinkhole scaling is scale-free or scale-bound. Our results provide a new basis for geohazard-related risk management at the eastern Dead Sea and a contribution to understanding of collapse sinkhole development more generally.

2 Study Area

2.1 The Dead Sea basin and lake level fall

The Dead Sea is a hypersaline terminal lake for the River Jordan and for several commonly dry river valleys (wadis) that drain the surrounding highlands (Fig. 1). The lake sits within an 80 km long and 5–17 km wide pull-apart basin, which has formed along the active, left-lateral Dead Sea Transform fault system (ten Brink and Flores, 2012; Garfunkel and Ben-Avraham, 1996). Deep boreholes and seismic reflection data show that the basin hosts a succession of siliciclastic, carbonate and evaporite rocks that is locally over 8 km thick (ten Brink and Flores, 2012; Neugebauer et al., 2014). Since the late Pleistocene, the Dead Sea basin's tectonic subsidence rate has been about 4.2 km Myr^{-1} (i.e. 4 mm yr^{-1}).

The shoreline of the Dead Sea is the deepest location on land on Earth – and increasingly so. Around 25 ka, the lake level reached a high stand of −162 m r.m.s.l. (Bartov et al., 2002; Goldsmith et al., 2023), i.e. it was about 250 m higher than today. At around 10–11 ka, the lake level may have declined to about −480 m r.m.s.l., in association with widespread halite deposition (Kiro et al., 2017). Subsequently, from around 6 ka, the Dead Sea level rose to about −410 m r.m.s.l. (Goldsmith et al., 2023), and it persisted at roughly this level to historical times. The lake level was at about −395 m r.m.s.l. in the 1970s, but since then it fell by about −0.5 m yr^{-1} in the 1980s and about −1.1 m yr^{-1} in the 2010s. The main cause of this recent decline is the diversion of freshwater sources for drinking water and irrigation (Yechieli, 2000). Due to its bathymetric characteristics, the Dead Sea has separated into northern and southern sub-basins either side of the prominent Lisan peninsula (Fig. 1b). The southern sub-basin has been further sub-divided by the construction of evaporation ponds, which are used to extract potash and other economically important minerals from the Dead Sea brine. As of 2022, the northern Dead Sea lake level was measured at −437 m relative to mean sea level (r.m.s.l.) – i.e. it has fallen by over 40 m since 1970 (Baer et al., 2023; Long-Term Changes in the Dead Sea, 2025).

As the Dead Sea level is the regional hydrogeological base level, its fall has had several geomorphologically important consequences both on and below the Earth's surface. On the surface, the Dead Sea shoreline has receded as the base level has fallen. Consequently, and depending on the pre-recession bathymetry, the former lakebed is in places exposed to shore-perpendicular widths of over 2.5 km (Fig. 2a–d). The former lakebed has undergone a wide-scale subsidence at rates of up to 30 cm yr^{-1}, dependent on time since its exposure and probably a result of dewatering-induced compaction (Baer et al., 2002; Fiaschi et al., 2017; Vey et al., 2021; Watson et al., 2019). The lacustrine sediments haveTS6 also undergone fluvial erosion; numerous stream channels have been carved into it as the surface (and subsurface) drainage system find new pathways to the lake (Fig. 2e–h) (Vachtman and

Proof Copy

Laronne, 2013). Furthermore, the steepening of the regional hydrological drainage gradient induced by the base level fall has caused TS7 deepening and shoreward incision of drainage channels into the pre-recession alluvial fan deposits marginal to the Dead Sea (Arkin and Gilat, 2000; Avni et al., 2016). Below the surface, the base level fall has caused changes in groundwater level, gradient and relative saturation that have generated a rapidly evolving evaporite karst system.

2.2 The Dead Sea evaporite karst system

Data from 40 shallow boreholes on the western shore of the Dead Sea basin have shown that the sinkholes form within the Ze'elim Formation, a 30–80 m thick sequence of flat-lying fluvio-lacustrine sediments of Holocene age (< 11 500 yr BP) (Stein et al., 2010; Yechieli et al., 1993). These sediments are characterised by laminated clay, silt and marl, which is interbedded with m-scale lenses of sand or conglomerate and with cm-scale to m-scale layers or lenses of evaporite minerals, such as aragonite, gypsum or halite (Migowski et al., 2006; Torfstein et al., 2008; Yechieli et al., 1993). In most of these boreholes, a massive halite layer, or a package of massive halite layers intercalated with clay, was found at or near to the Ze'elim Formation base. The age of this halite-rich section is bracketed to 10–11 ka based on radiocarbon dating of wood in the clay-rich deposits above and below it (Stein et al., 2010). The top surface of the salt-dominated section lies at elevations of −416 m to −449 m r.m.s.l., typically at a depth of 10–50 m below the present-day land surface. It varies in thickness from 2 to 23 m, with thickness broadly increasing seaward (Baer et al., 2023; Stein et al., 2010).

The main driver of sinkhole formation at the Dead Sea is dissolution (karstification) of this halite-rich section and the collapse of the overlying sedimentary cover into cavities generated within it (Avni et al., 2016; Yechieli et al., 2006). Piping or "subrosion", whereby water flowing through porous subsurface materials mechanically erodes the unconsolidated sands, clays and marls in the cover sequence, has been proposed as a complementary mechanism for cavity development and/or enlargement, particularly in the upper levels of the Ze'elim Formation (Al-Halbouni et al., 2017; Arkin and Gilat, 2000). The base level fall drives these processes by causing a corresponding decline of the groundwater table and a steepening of the subsurface hydraulic gradient in the land areas immediately around the Dead Sea (e.g. Abelson et al., 2017; Al-Halbouni et al., 2021). Additionally, the falling base level should in theory cause a lateral (seaward) shift of the interface between fresh and saline groundwater (Salameh and El-Naser, 2000; Yechieli, 2000), thus bringing subsurface salt-bearing deposits that were in chemical equilibrium with Dead Sea brine into contact with undersaturated groundwater and thereby initiating their dissolution. In practice, this density driven process may happen on more local, laterally variable scales (Avni et al., 2016; Rajab et al., 2025).

In addition to their long-term forcing from the base level fall, subsurface processes of erosion are influenced by long-term (multi-year) and short-term (days) variability in groundwater recharge, as rain falling on the surrounding highlands flows through the regional groundwater aquifers and through the wadis into the conduits of the subsurface karst system at the Dead Sea (Abelson et al., 2017; Al-Halbouni et al., 2021; Avni et al., 2016).

The subsurface erosion around the Dead Sea has produced three distinct forms of subsidence feature: sinkholes, compound sinkholes and uvalas. These features are found both in the former lakebed and in the adjacent alluvial fans. Previous work incorporating remote sensing analysis (Watson et al., 2019), fieldwork (Al-Halbouni et al., 2017, 2021) and modelling (Al-Halbouni et al., 2019) has demonstrated a clear distinction between these landforms at Ghor Al-Haditha, not only in terms of morphometry but also in terms of the processes involved in their genesis. The sinkholes are 1–80 m D TS8 enclosed depressions with width/depth ratios of 0.4–0.04 (Al-Halbouni et al., 2017; Filin et al., 2011; Watson et al., 2019). The sinkhole width/depth ratio is notably dependent on the mechanical properties of the near-surface material in which the sinkholes form. Sinkholes formed in alluvium have higher ratios (i.e. are deeper and/or narrower) compared to those formed in lacustrine mud, marl and salt (Al-Halbouni et al., 2017; Filin et al., 2011; Watson et al., 2019). A compound sinkhole forms when several individual sinkhole collapses coalesce and merge over the years into one larger and more irregularly shaped depression. The uvalas are 200–500 m D TS9 enclosed depressions with width/depth ratios of 0.04–0.01 (Avni et al., 2016; Watson et al., 2019). Each uvala includes numerous sinkholes. There is a close association in space and time between sinkhole and uvala development. To some degree the uvalas develop in association with compound sinkhole formation (Al-Halbouni et al., 2019; Sevil and Gutiérrez, 2023); however, the uvalas more typically have spatially distinct structural boundaries and they develop at a larger length scale (Watson et al., 2019). The sinkholes probably represent discrete collapses into individual subsurface karst conduits, whereas the uvalas represent more distributed subsidence across a karst conduit network (Watson et al., 2019).

2.3 The Ghor Al-Haditha sinkhole area

Our study area is in the southeast sector of the northern Dead Sea sub-basin, just east of the Lisan Peninsula (Fig. 1b). Two main wadis, the Wadi Ibn Hamad and the Wadi Mutayl, of which the former has by far the largest catchment (Al-Halbouni et al., 2021), terminate in the south of the study area (Fig. 2). Several smaller wadis descend from the escarpment of the Eastern Boundary Fault in the North of the area. Rainfall runoff from the highland plateau to the east flows through the wadis, typically in the form of flash floods, which in themselves represent a significant hazard in

Proof only

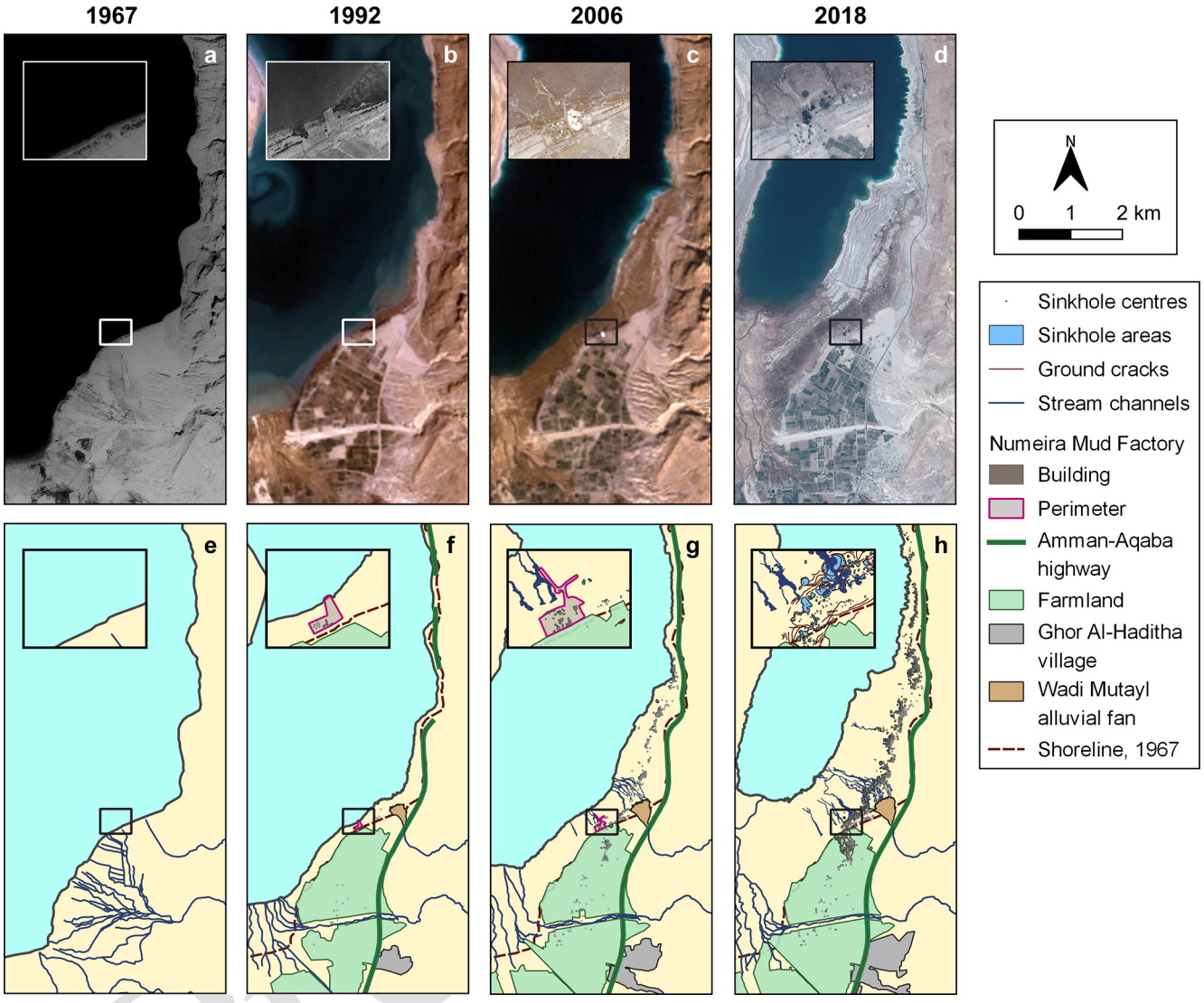


Figure 2. Historical land use development and geomorphological change at Ghor Al-Haditha over 50 years from 1967 to 2018. The upper panels **(a)**–**(d)** show satellite images for 1967, 1992, 2006, and 2018. The lower panels **(e)**–**(h)** highlight the land use development throughout those years. The insets highlight the development of the area around occupied by the now-destroyed Numeira mud factory. Base imagery is from the **(a)** Corona (USGS), **(b)**–**(c)** Landsat (USGS) and **(d)** Pléiades (© CNES 2024, Distribution Airbus DS) satellites.

the region (e.g. in 2018, a flash flood event at the Wadi Ma'in about 25 km north of the study area killed 21 persons, mostly schoolchildren). Over thousands of years, deposits from flash floods have accumulated at the mouths of the Ibn Hamad and Mutayl wadis to build a large alluvial fan of mainly unconsolidated to semi-consolidated sands and gravels.

The composition of the lacustrine sediments exposed in the former lakebed varies from south to north (Fig. 2d). In the south, the sediments exposed at the surface and in newly incised stream channels mostly comprise weakly to unconsolidated deposits of laminated marl, silt and clay, which are locally studded with cm-scale halite crystals. These soft fine materials are interbedded with harder layers of crystalline evaporites (aragonite, gypsum) that are 0.1–1 m thick. In general, the proportion of evaporite in the lakebed exposures increases seawards (Fig. 2d). In the north, the exposed lacustrine deposits are mostly evaporites – including rock salt (halite) – in 0.5–2.0 m thick layers interbedded with thin mud/marl layers.

The ages and true thicknesses of the fluvio-lacustrine deposits at Ghor Al-Haditha are imprecisely known, because of limited borehole control and a lack of radiometric ages. As the Dead Sea level has fallen from its "Lake Lisan" high stand at 25 ka, the alluvial fans have likely prograded westwards across and over older lacustrine deposits (El-Isa et al., 1995; Polom et al., 2018). Seismic reflection profiling indicates a ~ 200 m thick stack of lacustrine and alluvial deposits beneath the modern-day Ghor Al-Haditha fan (Al-Halbouni

et al., 2021; Polom et al., 2018). Logs from two boreholes drilled in the alluvial fan centre at elevations of ca. −380 and −386 m record a succession of sands and gravels to depths of 44 and 50 m, respectively, which is underlain by a 1–2 m thickness of greenish clay (El-Isa et al., 1995). Alluvium thickness diminishes to 1–2 m at the fan edges. The thickness of lacustrine deposits so far exposed by the recent lake recession is about 25 m. Intriguingly, the exposures of rock salt in the north of the area occur at elevations below −430 m (Fig. 3), which is close to the average elevation (−428 m) of the top of the basal halite-rich section of the Ze'elim Formation on the western shore (Baer et al., 2023). Based on their field characteristics and structural position, the lacustrine deposits exposed on the eastern shore are thus very likely to correlate to the Ze'elim Formation and to be of Latest Pleistocene to Holocene age (El-Isa et al., 1995; Bookman et al., 2004; Yechieli et al., 1993).

Sinkhole development in the Ghor Al-Haditha area has shown a remarkably systematic trend from 1990–2017 (Fig. 3). Sinkholes first formed there in the mid-1980s to the south of the Wadi Ibn Hamad and west of Ghor-Al Haditha village (El-Isa et al., 1995; Sawarieh et al., 2000; Taqieddin et al., 2000). Newer holes have since generally formed progressively further northward and seaward through time (Watson et al., 2019). Although not so pronounced, a similar pattern of seaward development of new sinkhole formation is also recorded at some localities on the western shore of the Dead Sea, e.g. Mineral Beach and Ze'elim (Abelson et al., 2017; Arav et al., 2020; Avni et al., 2016; Sevil and Gutiérrez, 2023). Such a systematic lateral migration is consistent with theoretical considerations of the migration of a saltwater-freshwater interface with base level fall (Al-Halbouni et al., 2021; Salameh and El-Naser, 2000; Watson et al., 2019), although direct evidence to test this hypothesis is absent (Rajab et al., 2025).

As new sinkholes developed further northwards in the early 1990s and 2000s, infrastructure, buildings and agricultural land have been affected (Al-Halbouni et al., 2017). Most notable is the abandonment and destruction between 2007 and 2010 of the Numeira mud factory northwest of Ghor Al-Haditha town (Fig. 2) (Watson et al., 2019). In addition, several fields, roads and houses in parts of the alluvial fan in agricultural land use have been damaged or destroyed. Since the 2010s, new sinkhole formation has increasingly focussed on the section of coastline closest to Highway 65, which is a major national road connecting the Jordanian capital city of Amman with that country's main port of Aqaba on the Red Sea (Fig. 3).

A systematic spatio-temporal development of evaporite karstification and sinkhole formation is helpful for qualitative or semi-quantitative forecasting of the likely location of new sinkholes (e.g. Galve et al., 2008, 2011). For the eastern Dead Sea shore, it might be anticipated that post-2017 sinkhole development would have continued to shift further north in the areas next to Highway 65 (Fig. 3). Subsidence from karstification, as well as erosional undercutting by stream channel incision, could in principle put this highway section at risk of damage or even closure, as has happened to several sections of a main coastal road on the Dead Sea's eastern shore (Arkin and Gilat, 2000; Watson et al., 2019). On the other hand, the apparent cessation or reduced rate of sinkhole formation in farmlands within the southern part of the Ghor Al-Haditha study area between 2010–2017 (Watson et al., 2019) might be interpreted as indicating a reduced hazard (and risk) to elements such as agricultural holdings, roadways and housing there. To help to evaluate hazard development, we undertook new mapping of the eastern shore via satellite remote sensing. Our goals were to establish whether the previous patterns of subsidence have persisted since 2017 and to assemble size distribution data for probabilistic forecasting of future sinkhole dimensions.

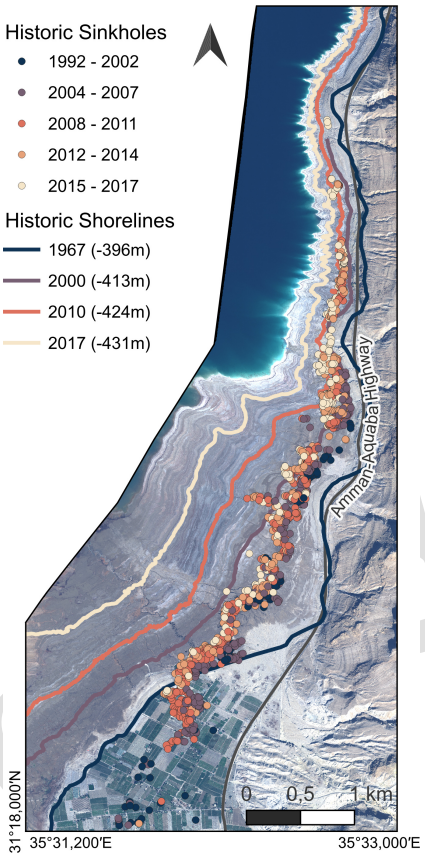


Figure 3. Evolution of shoreline position and sinkhole development within the Ghor Al-Haditha study area from 1992–2017 (modified from Watson et al., 2019). Base image is a Pleiades natural colour image acquired on 22 January 2024 (© CNES 2024, Distribution Airbus DS). Note the progressive shift in new sinkhole development northwards and seawards through time.

Proof

3 Data and Methods

3.1 Optical satellite and aerial imagery

To produce new data on sinkhole development at the Ghor Al-Haditha study site, we analysed ten high resolution satellite images captured between April 2018 and February 2024. These comprised seven Pleiades 1A/B images and three Pleiades Neo images. Each image has a panchromatic band with a spatial resolution or Ground Sampling Distance (GSD) of 50 or 30 cm px^{-1}, respectively (see Table S1 in the Supplement). The images were radiometrically calibrated and pre-orthorectified by the image supplier, Airbus. Pansharpening of 4 multispectral (RGBi) bands (GSD = 2 m px^{-1}) in each image to the panchromatic band resolution was carried out by using ArcGIS Pro.

We also reanalysed imagery spanning 1967–2017. This dataset includes: (i) panchromatic Corona satellite imagery from 1967–1970 with a GSD of $\sim$ 2.0 m px^{-1}; (ii) digitised, panchromatic or colour aerial survey imagery from 1981, 1992 and 2000 with a GSD of $\sim$ 1.0 m px^{-1}; (iii) panchromatic or multispectral (RGB or RGBi) satellite imagery from 2002–2017 with a GSD of 0.6–0.3 m px^{-1} (after pansharpening); and (iv) orthophoto mosaics and digital surface models of the study site derived from three close-range photogrammetric surveys undertaken during field work at the study site in the years 2014–2016 inclusive.

The satellite images acquired between 2002 and 2017 were orthorectified and pan-sharpened by using a combination of the ERDAS Imagine and PCI Geomatica software packages and by using standard algorithms (Watson et al., 2019). Orthorectification requires an external elevation reference. Throughout this study, we use digital elevation model (DEM) as the generic term for a gridded elevation reference dataset, and digital surface model (DSM) where the dataset explicitly represents the elevation of the topmost surface, including vegetation and (man-made) structures. The DEM, software and any additional georeferencing steps used for each satellite scene are listed in Table S2.

The photogrammetric[TS10] mosaics and DSMs derived from previous UAV surveys[TS11], have a GSD of 0.1 m px^{-1}. Their horizontal and vertical accuracies are: 2014 (10, 11 cm), 2015 (12, 17 cm) and 2016 (37, 31 cm). The UAV surveys and the structure-from-motion techniques used to derive the related data are documented by Al-Halbouni et al. (2017) and Watson et al. (2019). In brief, the workflow of the authors comprised of (1) image selection and downsampling of the photos taken by the drone and/or helikite balloon, (2) aligning the selected photos, (3) assigning ground control points, and (4) an optimization loop comprising of dense point cloud processing, model construction and error/-gap evaluation (cf. Fig. 4 in Al-Halbouni et al., 2017).

3.2 Sinkhole and uvala recognition elements in optical imagery

Mapping of enclosed depression boundaries by remote sensing can be done via many different methods and datasets, each with their own caveats (Šegina et al., 2018). Here we have mapped depressions manually, primarily from optical satellite imagery but also from DSM[TS12] data from 2014–2016[TS13]. This is a subjective process, which depends upon a trained mapper correctly interpreting the ground features visible in the imagery. For reproducibility, it is therefore important to describe the objective criteria by which sinkholes at the Dead Sea can be defined in optical imagery.

Sinkholes can be identified and delineated by changes in the following recognition elements (in order of decreasing importance) across space in one image and across time in between successive images (Fig. 4):

Shape: Sinkhole outlines (rims) tend to be equidimensional or slightly elongated in plan-view; long/short diameter ratios > 2.0 are rare (Watson et al., 2019). Although in detail (and thus in higher resolution imagery) some sections can be slightly irregular or rectilinear, sinkhole outlines are to a first order rounded or subrounded.

Shadow: Since sinkholes are topographic depressions, they should exhibit shadow when illuminated by low angle light. The satellite images used in this study were acquired at various times of the year, but almost all were acquired in the morning (Table S1). Solar illumination was thus generally at an angle of 14–34° from horizontal and generally from the east or southeast at an azimuth of 080-130. A sinkhole is characterised in these images by an area of shadow inside its eastern or southeastern rim and an area of brighter pixels inside its western or northwestern rim.

Tone/Colour: Sinkholes commonly show a different tone or colour in their centres compared outside of the sinkhole. The most striking difference arises when the sinkhole is filled with water. In panchromatic imagery, the water-filled sinkhole centre will be dark and uniform in tone. In natural colour imagery, the water can be yellow, orange, green, blue, navy, or (rarely) pink. In sinkholes formed in evaporite-dominated sediments, the darker water contrasts greatly with the surrounding white or light grey salt-rich deposits. Evaporation of saline water from a sinkhole can leave behind a salt deposit, which appears as a white zone inside the sinkhole rim or in the lower central part of the hole. In sinkholes formed in mud-rich sediments, such white rims or centres contrast sharply against the surrounding grey or dark brown mud.

Texture: Dry sinkholes commonly display a rough texture internally from collapse and disruption of the sed-

Proof only

imentary deposits. Water-filled sinkholes tend to have a smooth texture. Some sinkholes filled with relatively fresh (brackish) water have margins occupied by vegetation (reeds), which is seen in both colour (green) and texture (grassy-looking).

Association: Larger or deeper sinkholes are commonly associated with marginal fractures that tend to be orientated tangentially to the hole centre. Finally, since sinkholes tend to form in clusters with varying interhole distance, confidence in the recognition of a new sinkhole can be increased if it is located close to existing sinkholes.

In agricultural areas on the alluvial fan, artificial irrigation ponds could be mistaken for sinkholes based on their similarity regarding the above recognition elements and on their similarity in scale. The irrigation ponds are constructed by digging a hole in the alluvium and by using the excavated material to build an embankment around the hole. They can be distinguished from sinkholes based on the recognition elements of shadow, texture and association. TS14 The positive relief of the embankment around the artificial hole is usually visible in the patterns of shadow. Conversely to sinkholes, the irrigation ponds show a bright eastern or southeastern rim and a dark western or northwestern rim in the analysed images. The hole is commonly lined with plastic sheeting to make it watertight. Thus, the internal texture of a dry irrigation pond tends to be smooth even when the sheeting is removed. In terms of association, the irrigation ponds are typically located in the corners of fields (or former fields) and are usually close to a roadway for ease of access. Collectively, these attributes enable the distinction of irrigation ponds from sinkholes. In the exposed lakebed, there are locally some small-scale excavations of alluvium or mud that could also be confused with sinkholes. These excavations can be distinguished mainly by their association with (proximity to) other man-made features such as roadway embankments.

The uvalas are more subtle features, as they have a low subsidence to diameter ratio (Sevil and Gutiérrez, 2023; Watson et al., 2019). The uvalas are usually delimited by sets of ground cracks (crevasse) and faults that trend parallel to the depression boundary, rather than parallel to any individual sinkhole or sinkhole cluster. The ground cracks can be 0.1–1.0 m wide and 2.0–4.0 m deep when formed in alluvium or salt; they are more numerous but are more subtle in mud (Al-Halbouni et al., 2017; Watson et al., 2019). The faults are usually normal in slip-sense and commonly down-throw toward the uvala centre.

Uvala can be identified and delineated by changes in the following recognition elements:

Tone/Shadow: The ground cracks are recognisable as sharp, linear or arcuate strips of abrupt darkening in tone (shadow). The faults vary in appearance depending on orientation. Fault scarps facing toward the illumination direction (thus showing positive relief) are represented as narrow, rectilinear or curvilinear strips of brightened tones. Fault scarps facing away from the illumination direction (thus showing negative relief) are represented as narrow, rectilinear or curvilinear strips of darkened tones (shadow).

Pattern/Association: The ground cracks and faults form as parallel or near-parallel sets, which are in turn usually oriented around major clusters of sinkholes.

Based on the recognition elements described above, we established rules and guidelines to ensure consistency in mapping for accurate sinkhole identification and delineation of their outlines. We applied this rule set not only to the 2018–2024 satellite images, but also retrospectively to 1992–2017 images to ensure comparability across the entire inventory.

3.3 Mapping and geospatial analysis

Mapping and geospatial analysis was conducted within a Geographic Information System (GIS). We mainly used ArcGIS Pro versions 3.0–3.4; however, we used QGIS versions 3.22–3.34 for some operations. The identification and annotation of sinkholes involved a systematic process that started with the earliest image and progressed through subsequent ones. In many instances, a sinkhole is more clearly developed in a later image, and so previous images were rechecked for any evidence (shadowing; change in tone or colour, etc.) of the presence of that sinkhole at an earlier date. We mapped each sinkhole centre as a point, and we mapped each sinkhole perimeter (and thus its area) as a polygon by using the freehand mapping tool in ArcGIS Pro. Groundcracks delimiting uvalas were mapped as polylines. We performed additional post-processing, statistical analysis, and data visualisation in Python with the pandas (The pandas development team, 2024), NumPy (Harris et al., 2020), Matplotlib (Hunter, 2007) and seaborn (Waskom, 2021) libraries. While we mapped the development of sinkholes, compound sinkholes and uvalas, we focus in our statistical analysis on the individual sinkholes only.

We produced one polygon dataset comprising all sinkholes visible in each year's satellite imagery. Notably, this dataset treats a compound sinkhole, where multiple sinkholes over the years merged into one larger depression, as a singular polygon. New sinkholes that have nested within existing depressions ("redundant sinkholes"; Sevil and Gutiérrez, 2024) are not distinguished. This dataset captures the change in total sinkhole-affected area, through time, including the spread of sinkholes into areas previously unaffected by sinkholes, TS15 and thus the overall spread of the sinkhole hazard, with time. We derived a second polygon dataset of the outlines of all individual sinkholes including "redundant" sinkholes. Each sinkhole is represented only once and is assigned to the year of its formation based on our satellite imagery archive. This dataset captures the size distribu-

Proof only

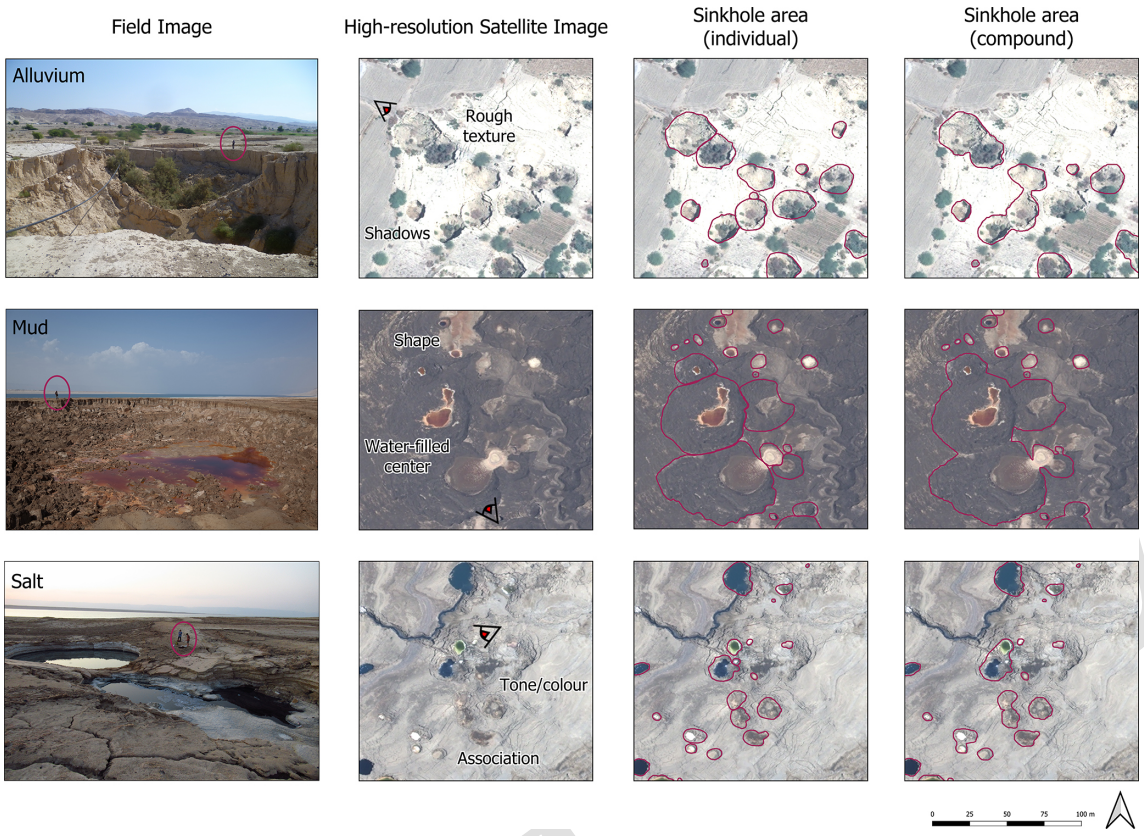


Figure 4. Example of the most prevalent identification features ("recognition elements") used for annotating sinkholes in different lithological units at Ghor Al-Haditha. The first column shows field photographs taken during past campaigns, illustrating the typical surface expressions of sinkholes in alluvium, mud, and salt-dominated substrates. Persons are circled in each for scale. The second column presents corresponding high-resolution satellite imagery, where key recognition elements are annotated. These include slope gradients inferred from wall shadows and debris infill (alluvium), water-filled centers and circular shapes (mud), and distinct tone, colour, and textural associations (salt). The third and fourth columns show the resulting sinkhole polygons (red outlines), delineated using these guidelines: either as individual sinkholes (third column) or as compound sinkholes (fourth column). Images in columns 2–4 are from the Pléiades Neo satellite (© Airbus DS 2024).

tion of the whole sinkhole population and the spatio-temporal dynamics of the sinkhole hazard in terms of the frequency-magnitude relationship.

From 1985–1999, several tens of sinkholes formed in farmlands were rapidly infilled. The Jordanian Ministry of Energy and Mineral Resources mapped the approximate locations and dimensions of 88 of these sinkholes through the analysis of aerial images, field campaigns and discussions with local farmers (El-Isa et al., 1995; Sawarieh et al., 2000, cf. Tables S3 and S4). These sinkholes have been omitted from our analysis as we could not verify their locations with remote sensing observations. Given their small number relative to the mapped population, however, this omission is unlikely to have impacted our overall results, and the scaling of this population subset indeed follows that of the main population overall. See Sect. S2 of the Supplement for a full appraisal of these data.

In some cases, it was challenging to delineate individual sinkholes in a compound sinkhole and to constrain the exact timing of each individual sinkhole collapse, especially when the compound sinkhole was water-filled. A sinkhole could be erroneously assigned to the wrong year because it may only become visible during dry periods in subsequent years. In some rare instances, vegetation growth obscured parts of sinkholes and made it challenging to estimate their dimensions accurately. Such issues caused by water and vegetation were nonetheless uncommon and affected only 1–5 sinkholes per image.

Two further sources of uncertainty apply across our new sinkhole datasets. The first is the ground sampling distance (GSD) of the source imagery, which links to the minimum mapping unit. For the period of sinkhole activity (mid 1980s to today), image resolution ranges from approximately 0.6 m for the earliest scenes to 0.3 m for the most recent. TS16 The second is subjective judgement of the operator performing the delineation. To gain some quantitative understanding of both factors, three representative zones spanning the salt, mud and alluvial substrates were mapped independently

Proof

by two operators (Watson and Schulten) from imagery of 2021 and 2022 that was resampled to 0.3, 0.6 and 2 m px^{-1} (Sect. S3, Figs. S3–S6). The two operators differed by an average of 11 % in point count and recovered a median of 80 % of the 0.3 m px^{-1} sinkhole count at 0.6 m px^{-1}, with loss at the lower resolution falling almost entirely on the smallest sinkholes. Since a sinkhole's size generally remains stable after its formation, sinkhole outlines seen in imagery from earlier years at 0.5–0.6 m px^{-1} could be corrected by reference to the later higher resolution imagery at 0.1–0.3 m px^{-1}. Moreover, the timing of small sinkholes with uncertain expression in earlier coarser imagery could be confirmed in the later high-resolution imagery. Hence, we consider the effect of these uncertainties on our principal results to be limited.

3.4 Sinkhole size-frequency analysis and exceedance probability calculations

We have primarily represented sinkhole size by the average of their maximum and minimum lengths (diameters). This eliminates the dimensionality scaling provided by sinkhole area, and we TS17 also show below that areas and lengths scale similarly. As the sinkholes at Ghor Al-Haditha are mostly near-circular in shape (Fig. S8), the average length is a close representation of the diameter of a circle of equivalent area. To find the maximum and minimum lengths of each sinkhole, we fitted a minimum bounding rectangle to its perimeter polygon in GIS and took the long and short sides of the rectangle. We chose to only analyse those sinkholes formed from 2004 to 2024, as this is the period for which we have the most precise chronological data.

We then tested if observed sinkhole size distributions fit by idealised power-law or log-normal distributions. A continuous, positive random variable x is distributed according to a power law relationship if:

$$f(x) = \frac{C}{x^{\alpha}} \tag{1}$$

where C is a normalisation constant and α is a constant scaling parameter. Power law distributions are "scale invariant", meaning that the distribution of x looks the same across all orders of spatial magnitude. Therefore, if the complementary cumulative distribution function (CCDF) of a variable following a power law distribution is plotted on a log-log plot, then it will appear as a straight line. In contrast, x is log-normally distributed if its logarithm ($\ln x$) follows the normal (Gaussian) distribution:

$$f(x) = \frac{1}{\sqrt{2\pi}\sigma} e^{-(\ln x - \mu)^2 / 2\sigma^2} \tag{2}$$

where μ and σ are the mean and standard deviation of $\ln x$ respectively (σ^2 being the variance). This means that if x is lognormally distributed, then $\ln x$ will follow the central limit theorem. For a lognormally distributed variable, μ and σ can thus be considered parameters giving information on the statistical location ("shift") and scale ("spread") of the distribution respectively.

To compare the fit of such idealised distributions to our sinkhole data, we used the "powerlaw" package within Python (Alstott et al., 2014). This package was written to facilitate robust and appropriate application of statistical methods for comparing the fit of heavy-tailed probability distributions to empirical data. Users can do this by visual inspection of the goodness of fit on a plot, and also by considering the loglikelihood ratio R between two candidate distributions. The R value for two distributions is calculated by performing a likelihood ratio test (also known as a Wilks test) to obtain a ratio of the goodness of fit for each candidate distribution, and then computing the natural logarithm of that ratio. If R is positive, the data more likely fits the first distribution, whilst if it is negative, the second distribution is a better fit.

We constructed empirical sinkhole formation frequency and size exceedance curves for sinkhole size (length or area), where the CCDF of sinkhole size represents the probability that a sinkhole randomly drawn from the sample exceeds a given size X. All such size-frequency and exceedance probability relationships are plotted on a log-log scale to highlight tail behaviour and facilitate detection of scale-invariance (if present). As a check, we additionally compared the μ and σ values of the lognormal distributions fitted by "powerlaw" with those obtained by using the SciPy package (scipy.stats.lognorm – SciPy v1.16.1 Manual, 2025; Virtanen et al., 2020).

Clauset et al. (2009) demonstrated that simply fitting a linear regression to empirical data plotted in log-log space is a statistically problematic way of establishing a power law relationship, since in practice most empirical data only obey a power law for values above a threshold (i.e. commonly for the upper tail of the distribution); this point was further underlined by Corral and González (2019). Clauset et al. (2009) proposed an updated method to fit a power-law to a given size distribution, which involves iteratively establishing the range of values across which a power law can robustly be fitted by minimising the Kolmogorov-Smirnov distance between the data and the fitted distribution. This method is encoded in "powerlaw" by Alstott et al. (2014) and so is used in our analysis.

4 Results

4.1 Spatio-temporal development of new sinkholes and uvalas from 2018 to 2024

The overall pattern of northward and seaward formation of new sinkholes at Ghor Al-Haditha has continued from 2018 to 2024 (Fig. 5). New sites of sinkhole formation have developed 2–3 km further north along the coastline than was visible in 2017. Sinkhole development continues to occur in clusters, which tend to precede uvala formation in a given

Proof only

area by several years. Three new uvalas (U6, U7, and U8) have formed in the north of the study area, with activity also shifting northwards with time as with the sinkholes, but with a time lag to initial sinkhole formation of several years.TS18 Ground cracks marking the eastern limits of U6 were visible from 2014–2017, leading to the suggestion of incipient uvala formation there (Watson et al., 2019). These cracks have since developed to form a fully enclosed uvala. Initial ground cracks delimiting uvalas U7 and U8 appeared in 2019, with significant developments in subsequent years. The newly formed northern uvalas straddle or sit next to the interface between the evaporite deposits and the alluvial fan deposits; they are (so far) more elongated and slenderer in shape than the older uvalas further south. The northerly shift in sinkhole formation with time has thus increased subsidence-related hazard next to the Amman-Aqaba highway (Fig. 6).

Further south, seaward expansion of the existing sinkhole areas around Uvalas U4, U3 and U2 has continued during 2018–2024 (Fig. 5). Sinkhole activity in and around uvala U2 (at the former Numeira mud factory site) had seemed to be waning prior to 2017, as no new ground cracks were observed there after 2014, either from remote sensing data or field observations (Al-Halbouni et al., 2021; Watson et al., 2019). From 2021, however, several new sinkholes and ground cracks have cut through agricultural fields to mark further seaward expansion of U2 to its southwest (see inset in Fig. 5). The more recently developed Uvala U6 also shows such a seawards expansion of new ground cracking and new collapse sinkholes. Since the early 2000s, the seaward expansion of the existing sinkhole affected areas has locally exceeded 500 m (Fig. 6).

Still further south, from the former Numeira mud factory site to around the Wadi Ibn Hamad, there has been a recent renewal of sinkhole formation. This area was originally active from 1992–2006, after which time sinkhole and uvala development there seemed to cease entirely. In particular, activity in the vicinity of U1 and the Wadi Ibn Hamad has also seen a revival since 2021, most notably since 2023, with at least 8–10 new sinkholes (Figs. 5 and 6) and potentially some renewed ground cracking (Fig. S7).

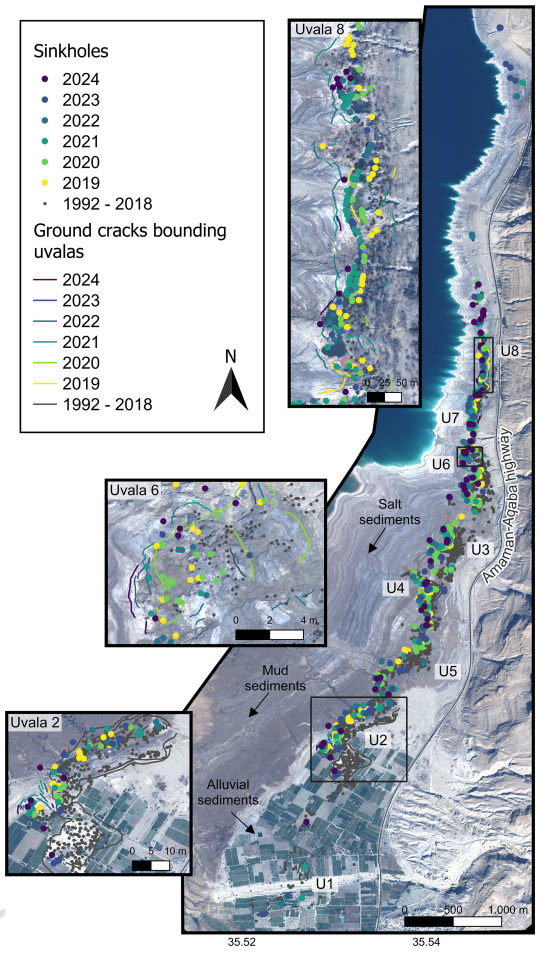


Figure 5. Spatio-temporal development of sinkholes and uvalas at Ghor Al-Haditha, 2018–2024. The background image is the 01.2024 Pléiades Neo satellite image (© Airbus DS 2024). The previously-identified northward and seaward trends of sinkhole migration are still apparent (cf. Watson et al., 2019). Alluvium, mud, and salt, the different sediments in which sinkholes form, are highlighted. Newly formed sinkholes are depicted in colour, while the smaller grey points symbolise older sinkholes (1992–2018).TS19

4.2 Growth trends of the sinkhole population from 1992 to 2024

The sinkhole population at Ghor Al-Haditha grew non-linearly from 1990 to 2004, but grew approximately linearly from 2004 to 2024 at a rate of ca. 100 new sinkholes per year (Fig. 7). Undercounting of sinkholes is unlikely to explain the initial non-linearity in the 1990–2004 interval for three reasons. First, image resolution is constant at $\sim 0.6\,\mathrm{m\,px^{-1}}$ from 1992 to 2007. Second, the number of holes mapped independently by the Jordanian MEMR in the 1990s does not differ sufficiently from our mapping of holes formed in the same interval (see Sect. S2). Lastly, a similar non-linear pattern of sinkhole count with time is seen for the mid 1980s to mid 2000s on the western Dead Sea shore also (Avni et al., 2016), even in areas where there is no agriculture or other activity to incentivise infilling of sinkholes. An evolution of the rate of sinkhole formation from non-linear to linear thus appears to be a fundamental feature of the Dead Sea karst system.

Our mapping yields a 43.6 % increase in the estimated total sinkhole population size at Ghor Al-Haditha locality, from 1565 holes in 2018 to 2247 holes in 2024 (Fig. 7). The growth of sinkhole-affected area has been less regular than that of sinkhole count. Area growth followed a similar trend to sinkhole count until 2009, but then underwent an unusually rapid expansion in 2009–2010 and a relatively slow expansion in 2015–2021. Total sinkhole area grew from $5096\,\mathrm{m^2}$ in 2000 to $46\,468\,\mathrm{m^2}$ in 2008, represent-

Proof

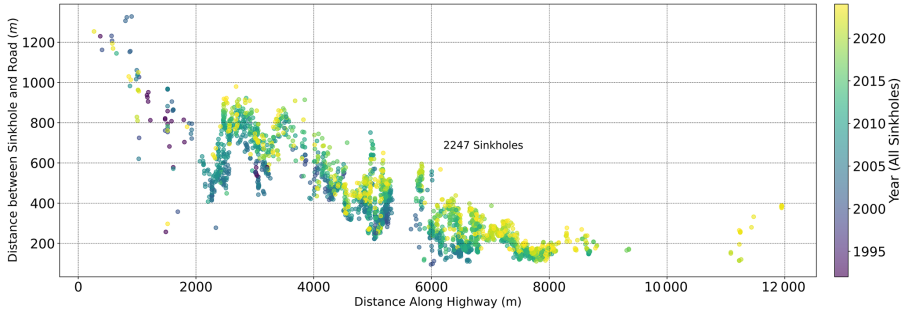


Figure 6. Scatterplot highlighting the potential threat the sinkhole pose to the highway. Over time, sinkholes have formed closer to the Amman-Aqaba highway. Distance from the centres of sinkholes to the road is plotted as a function of time (from the first observation of a given sinkhole instance). As sinkhole formation shifts towards the north of the study area, the proximity of the sinkholes to the Amman-Aqaba highway increases, and thus, so does the hazard posed by sinkhole formation to the highway. TS20

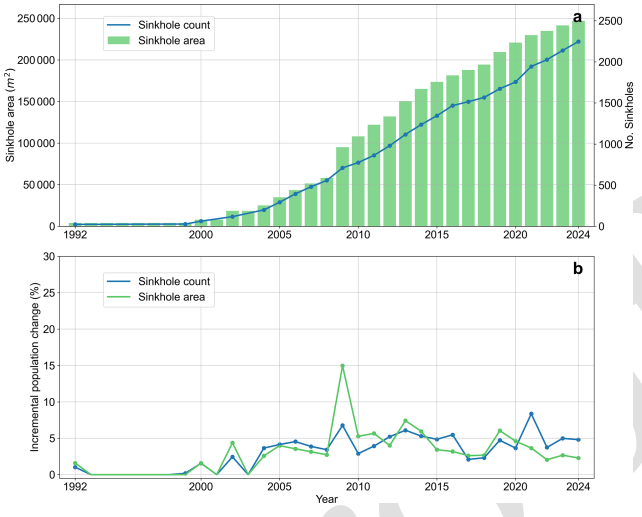


Figure 7. Temporal development of the sinkhole population at Ghor Al-Haditha. **(a)** Cumulative sinkhole population growth plotted in terms of the number of sinkholes and percentage increase in sinkhole area. Some years, such as 2009, show a significant increase in sinkhole development while the sinkhole area increased rapidly in the mid-2010s and has slowed down by the end of the study period. **(b)** Incremental sinkhole population growth plotted in percentage increase in sinkhole count and sinkhole area relative to their final totals. After a distinct period of rapid growth, sinkhole formation stagnated in the 2010s and has recently been picking up pace again. TS21 TS22

ing an average annual increase of $\sim 4890\,m^2\,yr^{-1}$. In 2009, the sinkhole-affected area more than doubled to $97\,468\,m^2$; this is by far the largest annual increase in sinkhole area recorded at the Ghor Al-Haditha site and represents 28 % of the entire area affected up until 2024. From 2009–2014, the total sinkhole area increased linearly by $\sim 9210\,m^2\,yr^{-1}$, but from 2014–2021, it slowed dramatically to $\sim 1230\,m^2\,yr^{-1}$. Finally, in the last 3 years, the sinkhole area growth accelerated again to $\sim 9150\,m^2\,yr^{-1}$ to reach a total sinkhole-affected area (excluding uvalas) of $179\,610\,m^2$ (i.e. nearly 18 ha, or $0.18\,km^2$) in 2024.

4.3 Distribution of sinkhole sizes

The distribution of sinkhole sizes for the entire population at Ghor Al-Haditha, as represented by the average length (diameter) of each sinkhole, TS23 is well represented by a log-normal distribution (Fig. 8). We tested that the logarithms of the data conform to the central limit theorem, which is a condition of the lognormal distribution, by plotting the distribution of the means of 50 random samples of the logs of 50 sinkhole lengths (Figs. S9 and S10). The Shapiro-Wilk statistics for these random samples are consistently above 0.97, indicating with near-certainty that the log values of sinkhole lengths at Ghor Al-Haditha are normally distributed. The log-normal distribution also applies if the sinkhole population is subsetted by the surface materials in which they are formed (alluvium, mud-rich lacustrine deposits, or evaporite-rich deposits). In general, sinkholes with an average length of 1–15 m are common. Sinkholes with average lengths of greater than 15 m or less than 1 m are rare. The maximum observed sinkhole length is 73 m and the minimum is 1 m. This size-frequency distribution closely accords with field observations of collapse sinkhole sizes as noted during our ground surveys in 2014–2016.

A lognormal distribution is also a far better fit to the full range of sinkhole size-frequency data than a power-law (Fig. 9). This is the case for average length, a power law is a very poor fit to the whole dataset in comparison to a lognormal distribution TS25 (Fig. 9a; loglikelihood ratio, $R = -1286$). Even if TS26 sinkhole area is considered, a log-normal distribution is still a far superior fit to a power law TS27 (Fig. 9b; $R = -1165$). A power law can equally well fit a portion of the dataset ($R \sim 0$) above a minimum length of 19.75 m or minimum area of $368\,m^2$. In this case, however, the power-law represents only the upper tail of the observed size range

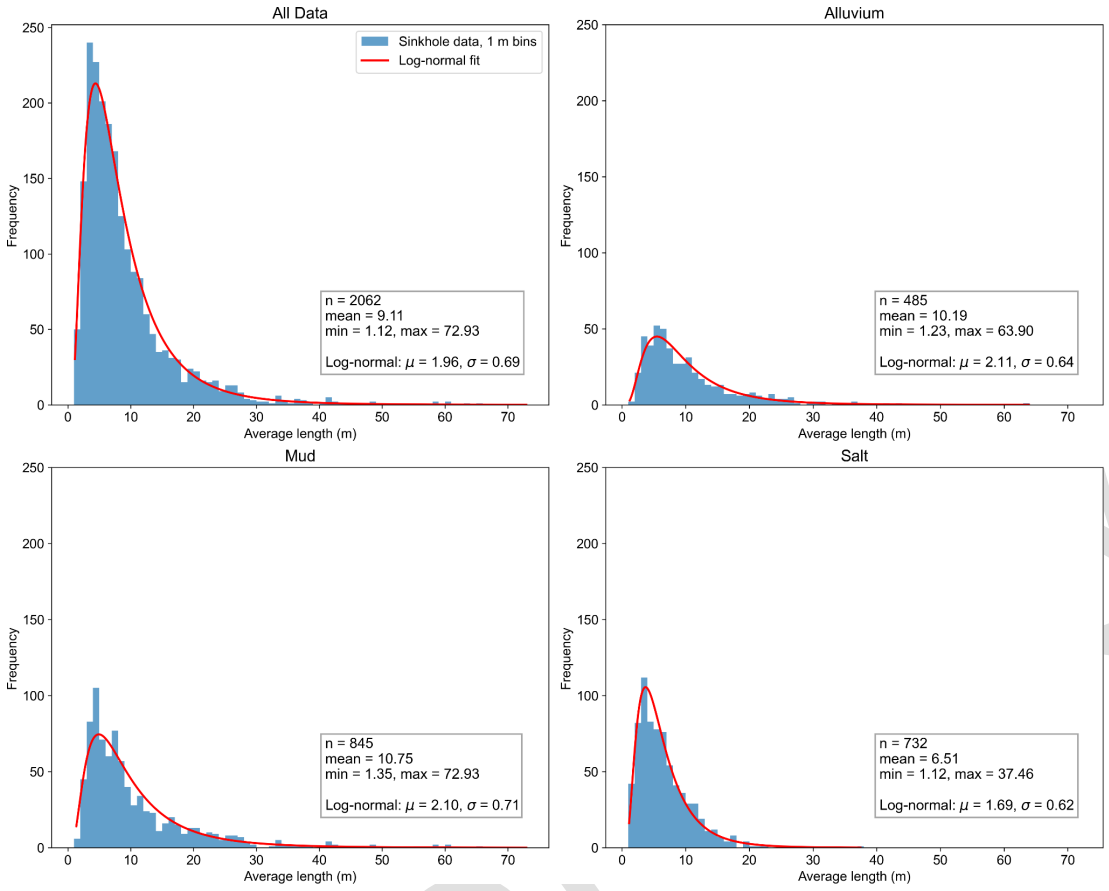


Figure 8. Sinkhole frequency-size distributions for the full 2004–2024 sinkhole population at Ghor Al-Haditha and for subsets of that population based on the type of near-surface sediment in which the sinkholes formed. TS24

(< 9 % of all observations), while the lognormal distribution represents the whole size range.

A lognormal distribution also provides a superior fit to the full ranges of sinkhole sizes when the population is subsetted according to the substrate material type (Fig. 10). Again, even for those scales where a power law provides a reasonable fit, a lognormal distribution can be fitted with comparable validity. Alluvium and mud sinkholes had a similar size cutoff for a good power-law fit ($x = 22.2$ and $x = 20.2$ m respectively), whilst salt sinkholes, being generally smaller (cf. Fig. 8), had a lower cutoff value of 10.5 m.

Annualised exceedance probability curves for the whole sinkhole population from 2004–2024 onwards (Fig. 11) can provide a quantitative estimation of future sinkhole hazard, under the assumption of a continuation of the behaviour documented above. Accordingly, the probability of a sinkhole with a length > 2 m (or area $> 3\,m^2$) forming in a given year is ~ 100 %, or near-certain. In contrast, the annualised exceedance probability for formation of a sinkhole with length > 10 m (area $> 80\,m^2$) is ~ 30 %, while for sinkhole with a length > 30 m (area $> 700\,m^2$) it is ~ 2 %. The probability of sinkhole collapse larger than 50 m in diameter (area $> 2000\,m^2$) in any given year is 0.3 %. These correspond to recurrence intervals (or return periods) of 1.0 TS30, 3.3, 50 and 1000 TS31 years, respectively.

The shape of the annualised exceedance probability curves remains consistent when alternatively calculated for 5-year intervals: 2004–2008, 2009–2014, 2015–2019 and 2020–2024 (Fig. 12). The sinkhole population at Ghor Al-Haditha thus followed lognormal size distributions throughout time. Changes in the distribution parameters nonetheless show subtle shifts in the dominant sinkhole size over time. The highest μ value (2.15) occurred in the period from 2009–2014, indicating the presence of comparatively larger holes in this data subset. This coincides with the notable development of many sinkholes of several 10's of m in diameter in the alluvial fan areas around the Numeira mud factory and nearby on the exposed mudflat (Figs. 3 and 4) and with the notable expansion in total sinkhole area at this time (Fig. 7). The following period from 2015–2019 had the lowest μ value at 1.77 (Fig. 12), meaning a decrease in the proportion of larger sinkholes, coincident with the northward migration of sinkholes formation into salt-dominated materials from the mid 2010s and the slowing down of the rate of the

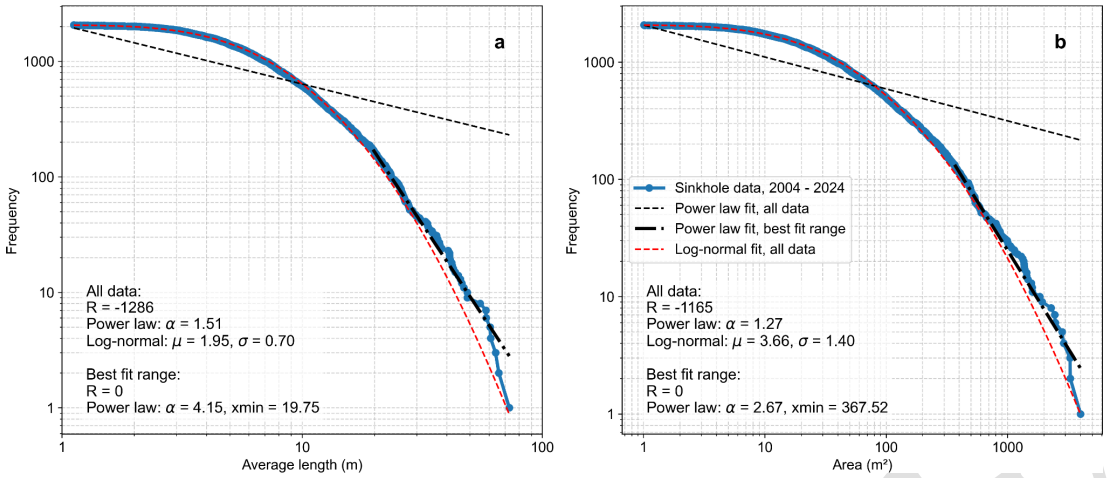


Figure 9. Cumulative frequency curves for **(a)** sinkhole average length (diameter) and **(b)** sinkhole area for all sinkholes formed in the period 2004–2024. Note that the values of μ and σ for the fitted lognormal distribution for average length **(a)** fitted by the "powerlaw" package are very close to the values obtained by fitting a lognormal distribution in the SciPy package (Fig. 8a), acting to further verify the robustness of the fit. In both cases, a power law fit can only be reasonably applied to the upper tail of the dataset (the larger sinkholes), whilst a lognormal fit reasonably approximates the entire distribution of sinkhole lengths and areas. TS28

area affected by sinkholes (Fig. 7). The most recent 5-year interval covering 2020–2024 shows a return to μ-value (1.92) (Fig. 12) more in line with that of the whole population (1.97) (Fig. 9a).

Although such changes of the cumulative frequency curves may appear subtle, they can have a significant impact on the estimated probability of sinkhole formation through time. For example, and for each 5-year interval, the probabilities of a collapse sinkhole of diameter greater than 10 m forming in a given year are: ~20 % (2004–2008), ~40 % (2009–2014), ~30 % (2015–2019), and ~20 % (2020–2024). For a collapse sinkhole of diameter greater than 30 m, the corresponding probabilities are: ~1.5 %, ~4 %, ~2.3 %, and ~0.7 %. Such temporal variations in the probabilities TS32 of sinkhole formation can thus lead to differences TS33 from those based on the whole 2004–2024 data set (30 % and 2 %, respectively) by a factor of 2 or 3.

5 Discussion

5.1 Past and future sinkhole hazard at the Dead Sea's eastern shore

A remarkable finding of this study is the continuation in 2018–2024 of the spatial migration of new sinkhole formation at Ghor Al-Haditha, in line with expectations based on past observations (Watson et al., 2019). New sinkhole development has continued to migrate northward into the evaporite deposits most recently exposed by the falling Dead Sea level. Furthermore, new sinkhole and uvala development in areas where such features were established prior to 2018 has since shown a pronounced seaward migration along the entire shoreline TS34 (Fig. 5). This spatio-temporal pattern of new sinkhole development has therefore persisted for over two decades. The observed overarching trends may reflect the large-scale lateral migration of a subsurface dissolution front within salt-rich deposits, with local areas of more rapid seaward advance representing localised hydrogeological "breakthrough" (Kaufmann et al., 2010). Ultimately, however, further work to constrain the geology, hydrogeology and hydrogeochemistry of the subsurface in the study area is required to test this hypothesis.

Based on the observed spatio-temporal pattern of sinkhole and uvala development, a key risk in the study area is damage or disruption of Highway 65 (The Jordan Valley Highway). Our mapping shows that since 2017 over 243 new sinkholes have formed within 250 m of the highway along a road-parallel distance of 3 km (Fig. 6). Within this section, two new uvalas (U7 & U8) have also developed, with some associated ground cracks located less than 100 m from the road. Given past behaviour, new sinkholes and uvalas might be expected to form also in the current "gap" between Uvala U8 and the new sinkholes formed since 2021 in the far north of the study area (Fig. 5). The hazard associated with subsidence is here combined with hazard from erosional undercutting downstream of the roadway by flash-flood stream flow through the several wadis crossed by road, with both processes ultimately linked to the ongoing base level fall. TS35

The renewal of sinkhole formation in the alluvium deposits in the southern part of the study area (Figs. 5, 6), where no significant changes were observed during 2010–2017 (Al-Halbouni et al., 2021; Watson et al., 2019), may be to some extent apparent. Sinkholes formed during the 2010–2017 period may have been infilled by farmers, and so not captured

Proof only

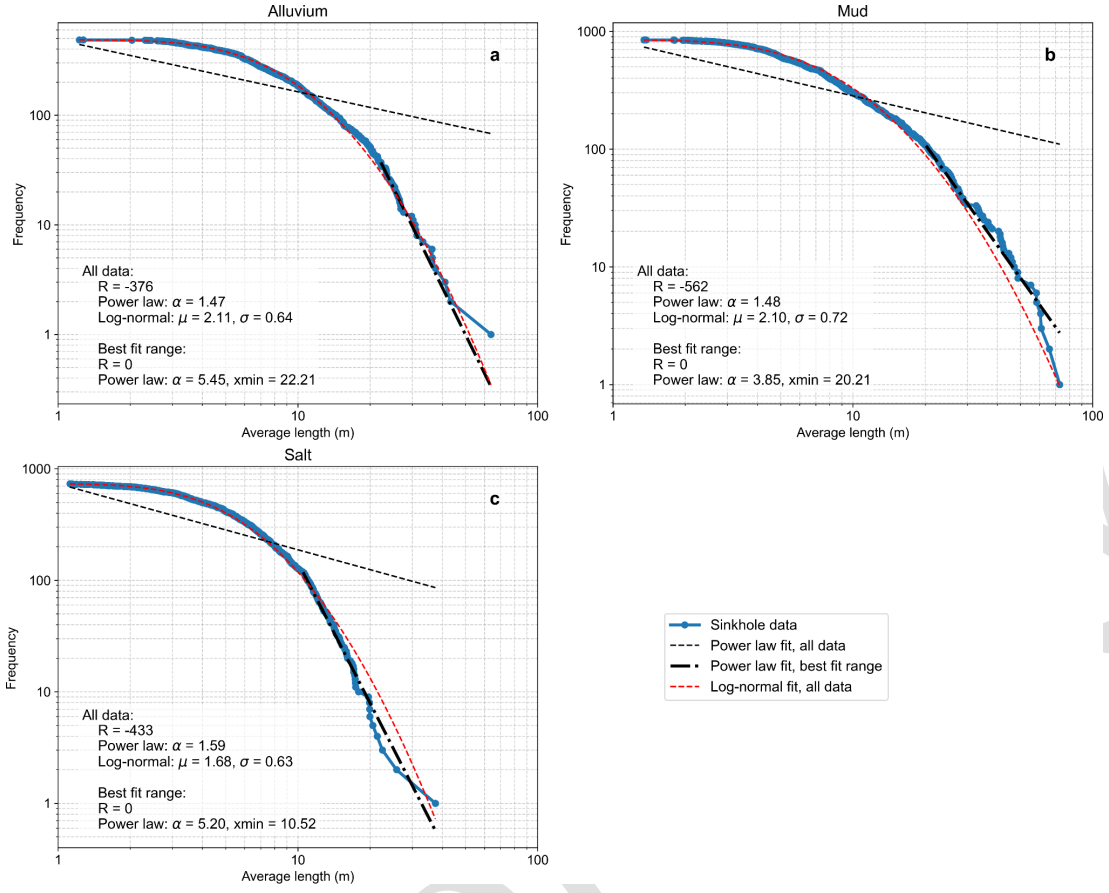


Figure 10. Cumulative frequency curves for sinkhole average length (diameter) as subdivided by the nature of the dominant sediment type in which the sinkholes formed: **(a)** Alluvium, **(b)** Mud and **(c)** Evaporite. Note that in each case the values of μ and σ for the lognormal distribution for average length fitted by the "powerlaw" package are very close to the values obtained by fitting a lognormal distribution in the SciPy software package (Fig. 8b–d), acting to further verify the robustness of the fit. In all cases, a power law fit can again only be reasonably applied to the tail of the dataset (the larger sinkholes), whilst a lognormal fit reasonably approximates the entire distribution of sinkhole lengths and areas. TS29

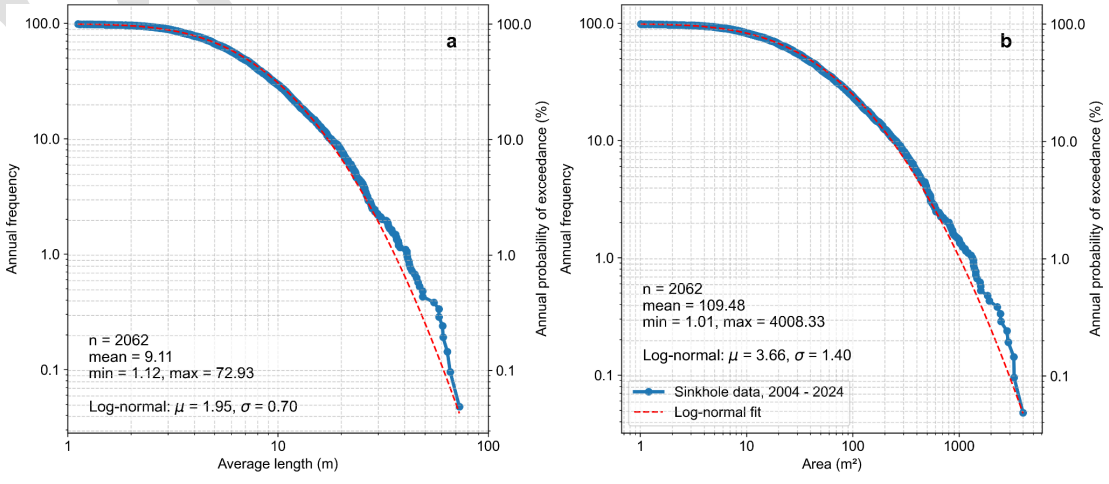


Figure 11. Annual frequency and annual probability of exceedance for the Ghor Al-Haditha sinkhole population from 2004 onwards, plotted by **(a)** average length and **(b)** area. Note that the upper limit of the left axis in each plot represents the time averaged rate of 100 sinkholes per year (see Fig. 7).

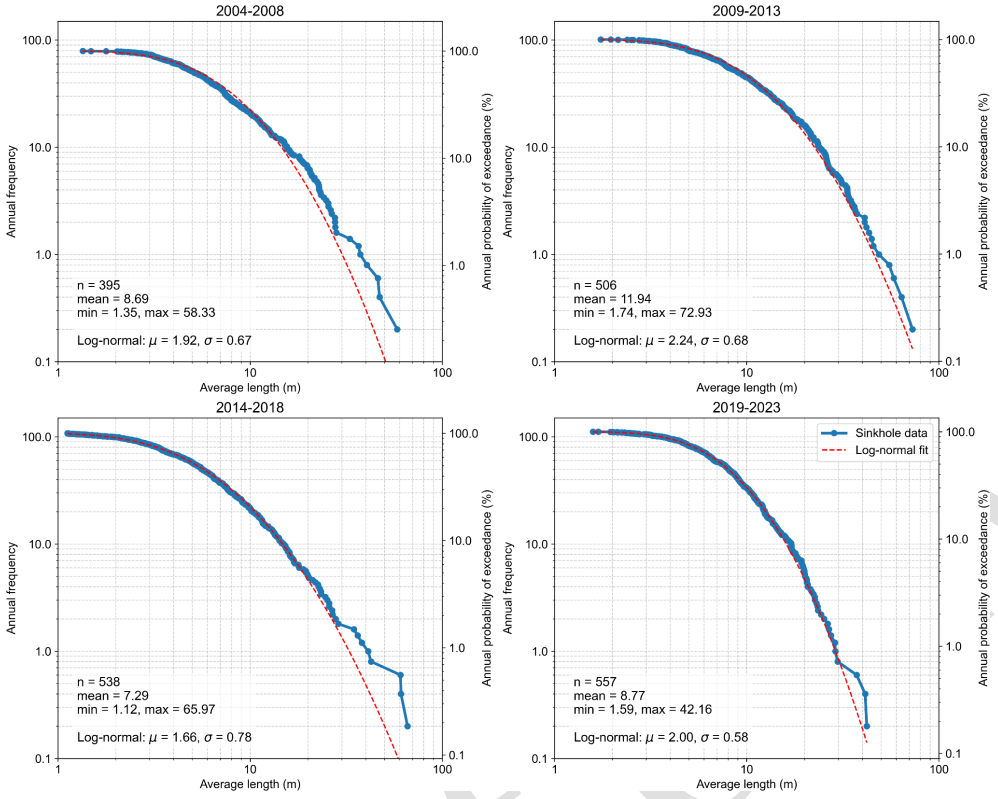


Figure 12. Annual frequency and annual probability of exceedance for the Ghor Al-Haditha sinkhole population in 5-year intervals from 2004–2024.

in annual satellite images (temporal aliasing). Alternatively, this renewal may be real and be driven by recent shifts in local groundwater flows, the nature and causes of which are unconstrained. Given its populated and agricultural nature, this part of the study area should undergo continued monitoring and further field/geotechnical investigation. Ultimately, our observations highlight the persistence of residual subsidence hazard and associated risks even in areas where sinkhole formation has apparently ceased.

For the first time in the Ghor Al-Haditha area, our cumulative frequency and exceedance probability analysis enables an estimation of the likelihood of sinkhole sizes that may form in future. Although sinkhole size distributions, and thus the exceedance probabilities generated from them, have varied in time (Fig. 12), the most recent activity seems to match the long-term population scaling (Fig. 11). Thus the annualised probability for formation of a hole of > 10 m D TS36, for example, is about 30 % adjacent to the Highway 65 section if based on the whole sinkhole population. If considering sinkhole formation in areas dominated by surface evaporite deposits, this probability of a new sinkhole exceeding 10 m D TS37 might alternatively be put at ~ 15 % (Fig. 10). This is not a full quantification of the hazards presented to infrastructure, given the other effects of broader subsidence (uvala development) and fluvial erosion. Furthermore, such forecasting depends on a continuation of the spatio-temporal patterns and size scaling so far observed, which is not guaranteed. Nonetheless, our updated mapping and probabilistic analysis can serve to give local authorities firmer data for evidence-based consideration of risk mitigation measures.

5.2 Metrics for Area Impacted by Sinkhole Hazards

Our results highlight the necessity of examining both sinkhole count and sinkhole-affected area to quantify the evolution of sinkhole hazard (see also Sevil and Gutiérrez, 2023, 2024). Although new instances of sinkhole formation have consistently numbered around 100 new holes per year since 2004, the growth in sinkhole-affected area is far more variable in time (Fig. 7). From the 5-yearly cumulative frequency curves (Fig. 12), this divergence between the growth trends of sinkhole count and area can be partly explained, in the first instance, as an increase in the proportion of large holes (> 10 m D TS38) in the 2009–2014 interval. For the subsequent 2015–2019 interval, when the expansion of sinkhole-affected area slowed markedly, an explanation in terms of an increase in the proportion of small holes is inconsistent with frequency-size data (Fig. 12). Instead, this slowdown in area expansion is caused by a greater concentration of newly formed sinkholes in areas where sinkhole clusters were already well established (Fig. 5; cf. Fig. 4, Watson et al., 2019)

– i.e. an increase in "spatially redundant" sinkholes, which in our mapping convention do not count toward the quantification of sinkhole-affected area.TS39 Therefore, while sinkhole count and dimensions are needed for a probabilistic understanding of hazard based on sinkhole population scalingTS40, a metric for sinkhole area that accounts for spatial redundancy is also important to assess the hazard extent and its evolutionTS41 (see also Sevil and Gutiérrez, 2023).

Sinkhole hazard can also be quantified in terms of the spatial density of new sinkholes, whereby the number of sinkholes or the number of sinkholes per year is normalised to an affected area (Sevil and Gutiérrez, 2023, 2024; Waltham et al., 2007). However, it is not always clear what the size of that area should be. One option is to use a bounding area of interest (e.g. Sevil and Gutiérrez, 2024), which is larger than the area occupied by sinkholes. As an example, for the 20 km^2 study area as a whole (Fig. 5), and for the ca. 2000 sinkholes formed in the 20 year period 2004–2024 (Fig. 7), we estimate an annualised density of new sinkholes of ca. 5 sinkholes km^{-2} yr^{-1}TS42. This compares to an annualised density of ca. 22 sinkholes km^{-2} yr^{-1}TS43 calculated for the 2 km^3 Ein Gedi site on the Dead Sea's western shore, where ca. 700 sinkholes formed within the 16 yr period 2005–2021 (Sevil and Gutiérrez, 2024). While this approach has the advantage of simplicity, the reported values are somewhat arbitrary as they depend on the chosen area and scale of interest. Moreover, it does not account for heterogeneity of sinkhole occurrence within the area of interest, although this can be addressed by density contour maps (e.g. Galve et al., 2011; Gökkaya et al., 2021). We have therefore opted to present the data here in the still simpler form of annualised sinkhole number, rather than annualised sinkhole density, but we note that conversions to the latter can be obtained readily for a given area or scale of interest.

5.3 Scaling of cover collapse sinkholes in evaporite karst at the Dead Sea

The size distribution of cover-collapse sinkholes on the Dead Sea's western shore has been previously considered to be well represented by a power-law and hence to be "scale-free" (Yizhaq et al., 2017). This conclusion was attained from an initial dataset of ca. 1300 holes (formed in 2002–2013 at 12 sites), from which the size distribution of a subset of 609 holes with a diameter greater than 5 m (area > 20 m^2) was modelled with a power law distribution (Yizhaq et al., 2017). The maximum sinkhole diameter included was 85 m (area ~5800 m^2). The size data considered thus spanned around 2.5 orders of magnitude in terms of sinkhole area, but less than 1.5 orders of magnitude in terms of sinkhole diameter. No measure of the goodness of fit of a power law distribution was provided and no trialling of alternative distributions was described. Corral and González (2019) re-examined the dataset used by Yizhaq et al. (2017). They determined that a simple power-law distribution fit well only to sinkhole sizes greater than 24 m in diameter (area > 440 m^2). Moreover, by undertaking likelihood tests, Corral and González (2019) demonstrated that the size-frequency data of all 1300 holes sampled on the western shore better follow a lognormal distribution. A lognormal distribution was also deemed to well fit the size distribution of ca. 670 sinkholes (formed 2005–2021 at the Ein Gedi site) on the western shore (Sevil and Gutiérrez, 2024), although again no alternative fits or testing thereof were presented.

For a new dataset of > 2000 cover-collapse sinkholes on the Dead Sea's eastern shore, we also find that a lognormal distribution is a good fit to the entire size-frequency dataset (Figs. 8, 9). This is true whether size is denoted by length or area (because of the high circularity of the sinkhole perimeters) and whether the surface material in which a sinkhole is formed is predominantly alluvium, mud or evaporite (Fig. 10). Our analysis also shows that a well-fitting power law relationship only applies well to the upper tail of the size-frequency distribution (sinkhole diameters greater than 10–20 m in a given substrate material), where it spans less than one order of magnitude. A power-law size distribution therefore does not well represent the entire sinkhole population (Fig. 9); a log-normal distribution provides a much better fit to the full dataset.

The strong deviation from power-law scaling at small collapse sinkhole sizes in our data is very unlikely to be a result of sampling bias. Firstly, the spatial resolution (ground sampling distance) of satellite images acquired after 2002, from which the vast majority (~90 %) of sinkhole dimensions were estimated (Fig. 7), is 0.6 to 0.3 m (Table S1). Based on at least 4 × 4 px for feature recognition, the Minimum Mapping Unit (MMU) in this imagery set ranges from ca. 2.5 to 1.2 m in diameter. Moreover, since there is little or no post-collapse modification, the dimensions of most holes could be ascertained/refined in the later higher resolution satellite imagery (MMU ~ 1.2 m D) and in stillTS44 higher resolution orthophoto mosaics (GSD 0.1 m; MMU 0.4 m DTS45). Thus the portion of the sinkhole size range below which deviation from power-law behaviour occurs (i.e. < 10–20 m DTS46) should have been well captured by the available imagery upon which our mapping is based. Secondly, we have observed from extensive walkovers around hundreds of sinkholes in the Ghor Al-Haditha area in 2014–2016 that collapse sinkholes smaller than 1–2 m in diameter are very rare (Al-Halbouni et al., 2017; Watson et al., 2019). We conclude therefore that the poor fit of a power-law distribution to the sinkhole size distribution cannot be explained by undersampling of cover-collapse sinkholes of < 10 m in diameter.

Collapse sinkholes formed in evaporite karst at the Dead Sea are therefore not scale-free; they are scale-bound. On both western and eastern Dead Sea shores, sinkhole sizes span nearly 3 orders of magnitude for diameter (0.3–85 m) and just over 4 orders of magnitude for area (Corral and González, 2019; Sevil and Gutiérrez, 2024; Yizhaq et al.,

Proof only

2017; this study). Unlike as predicted by a power law, the frequency of occurrence diminishes progressively for both very large (< 30 m D[TS47]) and very small (< 1 m D[TS48]) holes. A sinkhole collapse at the Dead Sea on a scale outside of either end of the observed size range, while not precluded by the data, is thus extremely unlikely.

The scale-bound nature of cover collapse sinkholes at the Dead Sea is a function of geometric and mechanical limits on the underlying genetic processes. Geometric factors include: (i) the depth and initial thickness of the halite-rich basal sequence of the Ze'elim Formation; (ii) the number and thickness of crystalline evaporite (aragonite, gypsum) layers relative to weaker clay/marl layers within the overlying lacustrine sediments; and (iii) the depth of the interface between hypersaline and undersaturated groundwater. In general, these key thicknesses and depths are constrained to within the range 0.1–100 m (Abelson et al., 2017; Baer et al., 2023; Migowski et al., 2006; Neugebauer et al., 2014; Yechieli et al., 2006). Mechanical factors include the strength of the subsurface materials to (i) inhibit collapse into small cavities or conduits, (ii) sustain sufficiently large cavities, into which shallower materials can ultimately collapse, (iii) prevent lateral enlargement of initial hole diameters by later wall failure (Al-Halbouni et al., 2018; Shalev and Lyakhovsky, 2012). These geometric and mechanical factors combine to limit both the maximum and the minimum sizes of sinkhole collapse possible in the Dead Sea evaporite karst system, and hence produce a log-normal size distribution.

5.4 Scaling of karst depressions and gravity-driven collapses more generally

To place our results in a broader context, we have compared the size-frequency distributions of sinkholes formed at Ghor Al-Haditha to those at several other sites, drawing from datasets collected in a variety of lithological contexts where a range of sinkhole formation processes have occurred[TS49] (Fig. 13). These other karst environments represent a continuum of lithologies and genetic processes, and include the Burren limestone karst in Ireland (Watson et al., 2019), the Slovenian limestone karst (Mihevc and Mihevc, 2021; Verbovšek and Gabor, 2019) and the Sivas gypsum karst in Turkiye (Gökkaya et al., 2021). In the Burren, sinkholes are mostly formed by surface dissolution, though cover suffosion, cover collapse, caprock collapse and bedrock collapse all contribute to sinkhole formation and morphology in some cases (cf. Watson et al., 2024, Table 2). In Slovenia, Mihevc and Mihevc (2021) mapped dolines across the entire country with a deep learning approach, and subsetted them according to genetic process; we have selected only the collapse dolines for analysis. Verbovšek and Gabor (2019) analysed a small karst area in Slovenia called Matarsko Podolje, delineating sinkhole boundaries manually in GIS. We have subsetted their data to examine only first-order (non-nested) solution dolines. In Sivas, sinkholes are formed by two dominant genetic processes: bedrock collapse and cover subsidence (Gökkaya et al., 2021). Again, we examined only non-compound sinkhole cases from Sivas.

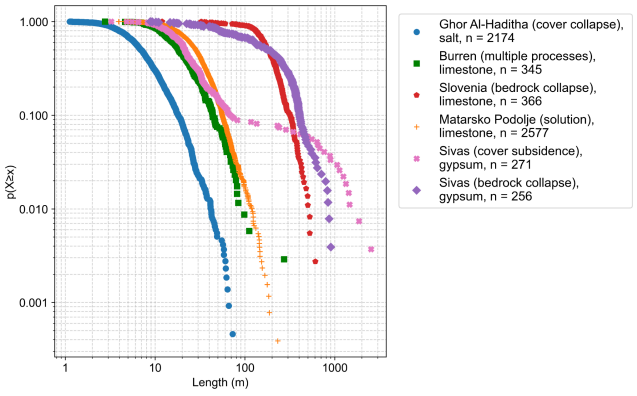


Figure 13. Comparison of size-frequency distribution of sinkholes formed at Ghor Al-Haditha with sinkhole (or doline) size-frequency data from other karst settings. Data are plotted as complementary cumulative distribution functions to enable easier comparison across the varying population sizes.

Sinkholes considered to have formed by collapse in these gypsum and limestone karst environments appear to have size-frequency distributions that are also well approximated by a lognormal distribution (Fig. 13). Again, a power law provides a good fit only to the upper tails of the data in these cases (Figs. S11–S14, Supplementary Material). Of the examples highlighted here, the lognormal approximation is closest fitting to the bedrock collapses in limestone karst (Slovenia) and gypsum karst (Sivas, Turkey). These bedrock collapse sinkholes are generally an order of magnitude larger than the cover collapse sinkholes in the Dead Sea evaporite karst. This observation could reflect greater material strengths and bounding scales (e.g. thicker karst rock formations, greater relief) in the gypsum and limestone karst areas. The cover collapse sinkhole data in gypsum karst (Sivas, Turkey) are anomalous in showing a 'terraced' size-frequency distribution, which reflects an abrupt increase of sinkholes of this type mapped in the diameter range 100–400 m. By analogy with the Dead Sea sinkholes, the Sivas dataset may represent processes limited by geometric or mechanical factors at two distinct scales.

Sinkholes considered to have formed mainly by surface dissolution ("solution sinkholes") in some limestone karst environments also have size-frequency distributions that appear to be better approximated by a log-normal distribution, rather than power-law (Figs. 13, S5, and S6). In the case of the Burren limestone karst in Ireland, a close control on the spatial distribution of sinkhole (dolines) is exerted by the stratigraphic and structural framework in which they form (Watson et al., 2024). A similar first-order control on spatial distribution from stratigraphic boundaries and structure (faults) is also evident in the case of the Matarsko podolje,

Proof only

Slovenia (Verbovšek and Gabor, 2019). Amongst other factors, these structural frameworks may play a role in limiting the lower and upper ends of size range of solution sinkholes. In other limestone karst areas, a lognormal function has been rejected as appropriate to model the size distribution of solution dolines, with a power-law preferred (e.g. Pardo-Igúzquiza et al., 2020). Ultimately a deeper discussion of the log-normal vs power-law scaling of solution dolines is beyond the scope of this work. We note, however, that if mapping (whether manual or automatic) is based primarily on remote sensing datasets, then a consideration of the MMU against a representative sample of field-measured sizes is critical to robust differentiation of either distribution at the lower end of the analysed size ranges.

The evolution of thinking regarding the size-frequency distribution of landslides, another gravity-driven collapse phenomenon, may be instructive for our wider understanding of the size-frequency distributions of collapse sinkholes. Landslide areas range across 3–5 orders of magnitude in several datasets collated globally, with simple power-law scaling being representative of only the upper 1–2 orders of magnitude (in some cases $< 25\,\%$ of the total number of observations) (Stark and Hovius, 2001). The ineffectiveness of a simple power-law distribution in describing the observed sizes at the lower end of the data range was initially attributed to strong undersampling ("censoring") at or below the MMU possible in the remote sensing data used to make the landslide inventories.TS50 Recent works with very high resolution data, thus extending the lower end of the observed range by an order of magnitude, have still reported inventories with a strong decline in landslide numbers at smaller sizes, however (Medwedeff et al., 2020). Such extended distributions are better approximated by a log-normal distribution (or double pareto distribution) than a simple power-law. Moreover this finding is explained as a consequence of geometric and mechanical (strength) factors limiting slope failure at small size scales (Medwedeff et al., 2020).

6 Conclusions

The rapid rate of cover collapse sinkhole formation at the Dead Sea provides a unique "natural laboratory" for testing scaling relationships and probabilistic hazard assessment in evaporite karst. The study area conditions, rarely met in karst environments, allow a collapse sinkhole population to be characterised without the confounding effects of erosional degradation, mixed genesis or unknown age. Exploiting this, and using high-resolution satellite imagery (Pleiades, PNEO) integrated with prior datasets, we present an updated inventory of sinkhole occurrence, extent and dimensions at the Dead Sea's eastern shore. We use the new inventory to test proposed scaling laws and to derive the first probabilistic hazard assessment for this area. Our main scientific findings are threefold:

1. Cover collapse sinkholes formed in evaporite karst at the Dead Sea are a scale-bound phenomenon. Sinkhole dimensions follow a log-normal size distribution. A power law fits only the upper tail of the observations. Field observations and minimum mapping unit considerations show that the inadequacy of a power-law fit is not due to undersampling of small sinkhole sizes.

2. Scale-bound behaviour enables a first quantitative hazard forecasting of sinkhole collapse at the eastern Dead Sea. Unlike for a power law, which implies scale-free behaviour, the log-normal scaling entails better defined minimum (ca. 1 m) and maximum (ca. 100 m) bounds to expected collapse sizes. Exceedance probabilities for a collapse of a given size vary slightly with sampling epoch and with the near-surface material in which collapse occurs.

3. Collapse sinkhole formation presents an still-evolving hazard to people and infrastructure in the Dead Sea region. New mapping at the Ghor Al-Haditha site confirms that the previously observed northward and seaward migration of sinkhole formation is continuing, Elements at risk include agricultural land, buildings and Highway 65. Localised resumption of sinkhole formation where it had seemingly ceased shows that residual subsidence hazard persists even in apparently inactive ground.

4. The scales of sinkhole collapse, and hence the hazard posed, are limited by the geometric and mechanical properties of the karst system. Beyond the Dead Sea, this contributes to a broader reassessment of the scaling of gravity-driven collapse phenomena.

Data availability. Data sets of the locations and outlines of the sinkholes as mapped in this study are available in an open-access online repository (https://doi.org/10.5281/zenodo.17417004TS51, Schulten et al., 2025). The Corona satellite images used in this work are available from the declassified imagery archives hosted online by the United States Geological Survey. The images acquired by the Quickbird, Worldview, Pleiades, and Pleases NEO satellites images are subject to commercial or academic licensing conditions; the original images cannot be shared with third parties under those conditions, but they are available at cost from several approved satellite imagery vendors. The aerial imagery from 1992 and 2000 is available at the discretion of the Royal Jordanian Geographical Centre. The UAV-based photogrammetric survey data from 2014–2016 (raw images, digital surface models and orthophoto mosaics) are available from the authors on reasonable request.

Interactive computing environment. .TS52

Supplement. The supplement related to this article is available online at [the link will be implemented upon publication].

Proof only

Author contributions. Schulten: Methodology, Investigation, Formal analysis, Data Curation, Visualization, Writing – Original Draft, Writing – Review & Editing. Watson: Methodology, Investigation, Validation, Formal analysis, Data Curation, Visualization, Writing – Original Draft, Writing – Review & Editing. Al-Halbouni: Data Curation, Writing – Review & Editing. Holohan: Conceptualization, Data Curation, Methodology, Writing – Original Draft, Writing – Review & Editing, Funding acquisition, Supervision, Project administration.

Competing interests. The contact author has declared that none of the authors has any competing interests.

Disclaimer. Publisher's note: Copernicus Publications remains neutral with regard to jurisdictional claims made in the text, published maps, institutional affiliations, or any other geographical representation in this paper. The authors bear the ultimate responsibility for providing appropriate place names. Views expressed in the text are those of the authors and do not necessarily reflect the views of the publisher.

Acknowledgements. We thank editor Paolo Tarolli and two anonymous reviewers for their constructive comments and queries, which helped us to sharpen several aspects of the manuscript. We acknowledge Ergin Gökkaya, Timotej Verbovšek and Rok Mihevc for sharing their sinkhole morphometric data with us. Discussions with Osama Alrabayah on mapping of the sinkholes at Ghor Al-Haditha are also appreciated. We are indebted to several members of the Jordanian Ministry of Minerals and Energy Resources (MEMR), in particular Dr Ali Sawarieh and Hussam Alrshdan, for guidance, hospitality and logistical support during field campaigns at Ghor Al-Haditha in 2014, 2015, 2016 and 2018. We also thank the many persons from Israel, Palestine, Jordan, Germany and elsewhere who organised, participated in or otherwise contributed to the Helmholtz Association's Dead Sea Research Venue (DESERVE) project (2013–2018) and who inspired our work on this beautiful and scientifically intriguing region.

Financial support. HZS conducted work at UCD while supported by an Erasmus+ Traineeship under supervision of EPH. RAW acknowledges a Government of Ireland Postgraduate Fellowship grant (Project ID: GOIPG/2020/790) for his PhD studies from the Irish Research Council (now Research Ireland), for which EPH acted as academic supervisor. EPH also acknowledges support for karst hazards research from the Research Ireland Centre for Applied Geosciences (iCRAG) (Grant Code: 13/RC/2092_P2).TS53

Review statement. This paper was edited by Paolo Tarolli and reviewed by two anonymous referees.

References

Abelson, M., Yechieli, Y., Baer, G., Lapid, G., Behar, N., Calvo, R., and Rosensaft, M.: Natural versus human controls on subsurface salt dissolution and development of thousands of sinkholes along the Dead Sea coast, J. Geophys. Res.-Earth Surf., 122, 1262–1277, https://doi.org/10.1002/2017JF004219, 2017.

Al-Halbouni, D., Holohan, E. P., Saberi, L., Alrshdan, H., Sawarieh, A., Closson, D., Walter, T. R., and Dahm, T.: Sinkholes, subsidence and subrosion on the eastern shore of the Dead Sea as revealed by a close-range photogrammetric survey, Geomorphology, 285, 305–324, https://doi.org/10.1016/J.GEOMORPH.2017.02.006, 2017.

Al-Halbouni, D., Holohan, E. P., Taheri, A., Schöpfer, M. P. J., Emam, S., and Dahm, T.: Geomechanical modelling of sinkhole development using distinct elements: model verification for a single void space and application to the Dead Sea area, Solid Earth, 9, 1341–1373, https://doi.org/10.5194/se-9-1341-2018, 2018.

Al-Halbouni, D., Holohan, E. P., Taheri, A., Watson, R. A., Polom, U., Schöpfer, M. P. J., Emam, S., and Dahm, T.: Distinct element geomechanical modelling of the formation of sinkhole clusters within large-scale karstic depressions, Solid Earth, 10, 1219–1241, https://doi.org/10.5194/se-10-1219-2019, 2019.

Al-Halbouni, D., Watson, R. A., Holohan, E. P., Meyer, R., Polom, U., Dos Santos, F. M., Comas, X., Alrshdan, H., Krawczyk, C. M., and Dahm, T.: Dynamics of hydrological and geomorphological processes in evaporite karst at the eastern Dead Sea – a multidisciplinary study, Hydrol. Earth Syst. Sci., 25, 3351–3395, https://doi.org/10.5194/hess-25-3351-2021, 2021.

Alstott, J., Bullmore, E., and Plenz, D.: powerlaw: A Python Package for Analysis of Heavy-Tailed Distributions, PLOS ONE, 9, e85777, https://doi.org/10.1371/journal.pone.0085777, 2014.

Arav, R., Filin, S., and Avni, Y.: Sinkhole swarms from initiation to stabilisation based on in situ high-resolution 3-D observations, Geomorphology, 351, 106916, https://doi.org/10.1016/j.geomorph.2019.106916, 2020.

Arkin, Y. and Gilat, A.: Dead Sea sinkholes – An ever-developing hazard, Environ. Geol., 39, 711–722, https://doi.org/10.1007/s002540050485, 2000.

Avni, Y., Lensky, N., Dente, E., Shviro, M., Arav, R., Gavrieli, I., Yechieli, Y., Abelson, M., Lutzky, H., Filin, S., Haviv, I., and Baer, G.: Self-accelerated development of salt karst during flash floods along the Dead Sea Coast, Israel, J. Geophys. Res.-Earth Surf., 121, 17–38, https://doi.org/10.1002/2015JF003738, 2016.

Baer, G., Schattner, U., Wachs, D., Sandwell, D., Wdowinski, S., and Frydman, S.: The lowest place on Earth is subsiding – An InSAR (interferometric synthetic aperture radar) perspective, Geol. Soc. Am. Bull., 114, 12–23, https://doi.org/10.1130/0016-7606(2002)114<0012:TLPOEI>2.0.CO;2, 2002.

Baer, G., Bernstein, M., Yechieli, Y., Nof, R. N., Abelson, M., and Gavrieli, I.: Elevation and thickness of the 11–10 Kyr old 'Sinkholes Salt' layer in the Dead Sea: clues to past limnology, paleo-bathymetry and lake levels, J. Paleolimnol., 70, 159–173, https://doi.org/10.1007/s10933-023-00286-9, 2023.

Bartov, Y., Stein, M., Enzel, Y., Agnon, A., and Reches, Z.: Lake Levels and Sequence Stratigraphy of Lake Lisan, the Late Pleistocene Precursor of the Dead Sea, Quat. Res., 57, 9–21, https://doi.org/10.1006/qres.2001.2284, 2002.

Proof Only

Bookman, R., Enzel, Y., Agnon, A., and Stein, M.: Late Holocene levels of the Dead Sea, Geol. Soc. Am. Bull., 116, 555–571, https://doi.org/10.1130/B25286.1, 2004.

Clauset, A., Shalizi, C. R., and Newman, M. E. J.: Power-law distributions in empirical data, SIAM Rev., 51, 661–703, https://doi.org/10.1137/070710111, 2009.

Cooper, A. H.: Halite karst geohazards (natural and man-made) in the United Kingdom, Environ. Geol., 42, 505–512, https://doi.org/10.1007/s00254-001-0512-9, 2002.

Corral, Á. and González, Á.: Power Law Size Distributions in Geoscience Revisited, Earth Space Sci., 6, 673–697, https://doi.org/10.1029/2018EA000479, 2019.

De Waele, J., Gutiérrez, F., Parise, M., and Plan, L.: Geomorphology and natural hazards in karst areas: A review, Geomorphology, 134, 1–8, https://doi.org/10.1016/j.geomorph.2011.08.001, 2011.

El-Isa, Z., Rimawi, O., Jarrar, G., Abou Karaki, N., Taqieddin, S., Atallah, M., Seif El-Din, N., and Al Saed, A.: Assessment of the hazard of subsidence and sinkholes in Ghor Al-Haditha area, 1995.

Fiaschi, S., Closson, D., Abou Karaki, N., Pasquali, P., Riccardi, P., and Floris, M.: The complex karst dynamics of the Lisan Peninsula revealed by 25 years of DInSAR observations. Dead Sea, Jordan, ISPRS J. Photogramm. Remote Sens., 130, 358–369, https://doi.org/10.1016/j.isprsjprs.2017.06.008, 2017.

Filin, S., Baruch, A., Avni, Y., and Marco, S.: Sinkhole characterization in the Dead Sea area using airborne laser scanning, Nat. Hazards, 58, 1135–1154, https://doi.org/10.1007/s11069-011-9718-7, 2011.

Galve, J. P., Bonachea, J., Remondo, J., Gutiérrez, F., Guerrero, J., Lucha, P., Cendrero, A., Gutiérrez, M., and Sánchez, J. A.: Development and validation of sinkhole susceptibility models in mantled karst settings. A case study from the Ebro valley evaporite karst (NE Spain), Eng. Geol., 99, 185–197, https://doi.org/10.1016/j.enggeo.2007.11.011, 2008.

Galve, J. P., Gutiérrez, F., Lucha, P., Bonachea, J., Remondo, J., Cendrero, A., Gutiérrez, M., Gimeno, M. J., Pardo, G., and Sánchez, J. A.: Sinkholes in the salt-bearing evaporite karst of the Ebro River valley upstream of Zaragoza city (NE Spain): Geomorphological mapping and analysis as a basis for risk management, Geomorphology, 108, 145–158, https://doi.org/10.1016/j.geomorph.2008.12.018, 2009.

Galve, J. P., Remondo, J., and Gutiérrez, F.: Improving sinkhole hazard models incorporating magnitude–frequency relationships and nearest neighbor analysis, Geomorphology, 134, 157–170, https://doi.org/10.1016/j.geomorph.2011.05.020, 2011.

Garfunkel, Z. and Ben-Avraham, Z.: The structure of the Dead Sea basin, Tectonophysics, 266, 155–176, https://doi.org/10.1016/S0040-1951(96)00188-6, 1996.

Gökkaya, E., Gutiérrez, F., Ferk, M., and Görüm, T.: Sinkhole development in the Sivas gypsum karst, Turkey, Geomorphology, 386, 107746, https://doi.org/10.1016/j.geomorph.2021.107746, 2021.

Goldsmith, Y., Cohen, O., Stein, M., Torfstein, A., Kiro, Y., Kushnir, Y., Bartov, Y., Ben-Moshe, L., Frumkin, A., Lensky, N. G., Keinan, J., Gonen, L., and Enzel, Y.: Holocene humid periods of the Levant – evidence from Dead Sea lake-levels, Quat. Sci. Rev., 318, 108312, https://doi.org/10.1016/j.quascirev.2023.108312, 2023.

Gutiérrez, F.: Sinkhole Hazards, in: Oxford Research Encyclopedia of Natural Hazard Science, https://doi.org/10.1093/acrefore/9780199389407.013.40, 2016.

Gutiérrez, F., Cooper, A. H., and Johnson, K. S.: Identification, prediction, and mitigation of sinkhole hazards in evaporite karst areas, Environ. Geol., 53, 1007–1022, https://doi.org/10.1007/s00254-007-0728-4, 2008.

Gutiérrez, F., Parise, M., De Waele, J., and Jourde, H.: A review on natural and human-induced geohazards and impacts in karst, Earth-Sci. Rev., 138, 61–88, https://doi.org/10.1016/j.earscirev.2014.08.002, 2014.

Gutiérrez, F., Fabregat, I., Roqué, C., Carbonel, D., Zarroca, M., Linares, R., Yechieli, Y., García-Arnay, Á., and Sevil, J.: Sinkholes in hypogene versus epigene karst systems, illustrated with the hypogene gypsum karst of the Sant Miquel de Campmajor Valley, NE Spain, Geomorphology, 328, 57–78, https://doi.org/10.1016/j.geomorph.2018.12.003, 2019.

Harris, C. R., Millman, K. J., van der Walt, S. J., Gommers, R., Virtanen, P., Cournapeau, D., Wieser, E., Taylor, J., Berg, S., Smith, N. J., Kern, R., Picus, M., Hoyer, S., van Kerkwijk, M. H., Brett, M., Haldane, A., del Río, J. F., Wiebe, M., Peterson, P., Gérard-Marchant, P., Sheppard, K., Reddy, T., Weckesser, W., Abbasi, H., Gohlke, C., and Oliphant, T. E.: Array programming with NumPy, Nature, 585, 357–362, https://doi.org/10.1038/s41586-020-2649-2, 2020.

Hunter, J. D.: Matplotlib: A 2D Graphics Environment, Comput. Sci. Eng., 9, 90–95, https://doi.org/10.1109/MCSE.2007.55, 2007.

Israel Marine Data Center (ISRAMAR): Long-Term Changes in the Dead Sea, https://isramar.ocean.org.il/isramar2009/DeadSea/LongTerm.aspx, last access: 16 May 2025. TS54

Johnson, K. S.: Evaporite-karst problems and studies in the USA, Environ. Geol., 53, 937–943, https://doi.org/10.1007/s00254-007-0716-8, 2008.

Kaufmann, G., Romanov, D., and Hiller, T.: Modeling three-dimensional karst aquifer evolution using different matrix-flow contributions, J. Hydrol., 388, 241–250, https://doi.org/10.1016/j.jhydrol.2010.05.001, 2010.

Kiro, Y., Goldstein, S. L., Garcia-Veigas, J., Levy, E., Kushnir, Y., Stein, M., and Lazar, B.: Relationships between lake-level changes and water and salt budgets in the Dead Sea during extreme aridities in the Eastern Mediterranean, Earth Planet. Sci. Lett., 464, 211–226, https://doi.org/10.1016/j.epsl.2017.01.043, 2017.

Medwedeff, W. G., Clark, M. K., Zekkos, D., and West, A. J.: Characteristic landslide distributions: An investigation of landscape controls on landslide size, Earth Planet. Sci. Lett., 539, 116203, https://doi.org/10.1016/j.epsl.2020.116203, 2020.

Migowski, C., Stein, M., Prasad, S., Negendank, J. F. W., and Agnon, A.: Holocene climate variability and cultural evolution in the Near East from the Dead Sea sedimentary record, Quat. Res., 66, 421–431, https://doi.org/10.1016/j.yqres.2006.06.010, 2006.

Mihevc, A. and Mihevc, R.: Morphological characteristics and distribution of dolines in Slovenia, a study of a lidar-based doline map of Slovenia, Acta Carsol., 50, https://doi.org/10.3986/ac.v50i1.9462, 2021.

Neugebauer, I., Brauer, A., Schwab, M. J., Waldmann, N. D., Enzel, Y., Kitagawa, H., Torfstein, A., Frank, U., Dulski, P., Agnon, A.,

Proof Only

Ariztegui, D., Ben-Avraham, Z., Goldstein, S. L., and Stein, M.: Lithology of the long sediment record recovered by the ICDP Dead Sea Deep Drilling Project (DSDDP), Quat. Sci. Rev., 102, 149–165, https://doi.org/10.1016/j.quascirev.2014.08.013, 2014.

Nof, R., Abelson, M., Raz, E., Magen, Y., Atzori, S., Salvi, S., and Baer, G.: SAR Interferometry for Sinkhole Early Warning and Susceptibility Assessment along the Dead Sea, Israel, Remote Sens., 11, 89, https://doi.org/10.3390/rs11010089, 2019.

Pardo-Igúzquiza, E., Dowd, P. A., and Telbisz, T.: On the size-distribution of solution dolines in carbonate karst: Log-normal or power model?, Geomorphology, 351, 106972, https://doi.org/10.1016/j.geomorph.2019.106972, 2020.

Polom, U., Alrshdan, H., Al-Halbouni, D., Holohan, E. P., Dahm, T., Sawarieh, A., Atallah, M. Y., and Krawczyk, C. M.: Shear wave reflection seismic yields subsurface dissolution and subrosion patterns: application to the Ghor Al-Haditha sinkhole site, Dead Sea, Jordan, Solid Earth, 9, 1079–1098, https://doi.org/10.5194/se-9-1079-2018, 2018.

Rajab, J. A., Yogeshwar, P., Tezkan, B., and Al-Halbouni, D.: Transient electromagnetic imaging of saltwater intrusion at the shrinking Dead Sea, Sci. Rep., 15, 30250, https://doi.org/10.1038/s41598-025-15189-0, 2025.

Salameh, E. and El-Naser, H.: Changes in the Dead Sea Level and their Impacts on the Surrounding Groundwater Bodies, Acta Hydrochim. Hydrobiol., 28, 24–33, https://doi.org/10.1002/(SICI)1521-401X(200001)28:1<24::AID-AHEH24>3.0.CO;2-6, 2000.

Sawarieh, A., Al Addas, A., Al Bashish, M., and Al Seba'i, E.: Sinkholes Phenomena At Ghor Al Haditha Study Area – Internal Report No. 12, Natural Resources Authority, Amman, Jordan, 2000.

Schulten, H. Z., Watson, R. A., Al-Halbouni, D., Alrabayah, O., and Holohan, E.: Locations and outlines of collapse sinkholes formed from 1992 to 2024 in evaporite karst at the eastern Dead Sea shore (Jordan) as defined in high resolution optical remote-sensing data, Zenodo [data set], https://doi.org/10.5281/zenodo.17417004TS55, 2025.

scipy.stats.lognorm – SciPy v1.16.1 Manual, The SciPy Project, https://docs.scipy.org/doc/scipy/reference/generated/scipy.stats.lognorm.html#scipy.stats.lognorm, last access: 31 July 2025.

Šegina, E., Benac, Č., Rubinić, J., and Knez, M.: Morphometric analyses of dolines – the problem of delineation and calculation of basic parameters, Acta Carsol., 47, https://doi.org/10.3986/ac.v47i1.4941, 2018.

Sevil, J. and Gutiérrez, F.: Morphometry and evolution of sinkholes on the western shore of the Dead Sea. Implications for susceptibility assessment, Geomorphology, 434, 108732, https://doi.org/10.1016/j.geomorph.2023.108732, 2023.

Sevil, J. and Gutiérrez, F.: Temporal variability of sinkhole hazard illustrated in the western shore of the Dead Sea, Nat. Hazards, 120, 12663–12677, https://doi.org/10.1007/s11069-024-06708-9, 2024.

Shalev, E. and Lyakhovsky, V.: Viscoelastic damage modeling of sinkhole formation, J. Struct. Geol., 42, 163–170, https://doi.org/10.1016/j.jsg.2012.05.010, 2012.

Shaqour, F.: Hydrogeologic role in sinkhole development in the desert of Kuwait, Environ. Geol., 23, 201–208, https://doi.org/10.1007/BF00771789, 1994.

Stark, C. P. and Hovius, N.: The characterization of landslide size distributions, Geophys. Res. Lett., 28, 1091–1094, https://doi.org/10.1029/2000GL008527, 2001.

Stein, M., Torfstein, A., Gavrieli, I., and Yechieli, Y.: Abrupt aridities and salt deposition in the post-glacial Dead Sea and their North Atlantic connection, Quat. Sci. Rev., 29, 567–575, https://doi.org/10.1016/j.quascirev.2009.10.015, 2010.

Taheri, K., Mohseni, H., Raeisi, E., and Taheri, M.: Sinkhole susceptibility mapping using the analytical hierarchy process (AHP) and magnitude–frequency relationships: A case study in Hamadan province, Iran, Geomorphology, 234, https://doi.org/10.1016/j.geomorph.2015.01.005, 2015.

Taqieddin, S. A., Abderahman, N. S., and Atallah, M.: Sinkhole hazards along the eastern Dead Sea shoreline area, Jordan: a geological and geotechnical consideration, Environ. Geol., 39, 1237–1253, https://doi.org/10.1007/s002549900095, 2000.

ten Brink, U. S. and Flores, C. H.: Geometry and subsidence history of the Dead Sea basin: A case for fluid-induced mid-crustal shear zone?, J. Geophys. Res.-B Solid Earth, 117, https://doi.org/10.1029/2011JB008711, 2012.

The pandas development team: pandas-dev/pandas: Pandas, Zenodo, https://doi.org/10.5281/zenodo.13819579, 2024.

Torfstein, A., Gavrieli, I., Katz, A., Kolodny, Y., and Stein, M.: Gypsum as a monitor of the paleo-limnological–hydrological conditions in Lake Lisan and the Dead Sea, Geochim. Cosmochim. Acta, 72, 2491–2509, https://doi.org/10.1016/j.gca.2008.02.015, 2008.

Vachtman, D. and Laronne, J. B.: Hydraulic geometry of cohesive channels undergoing base level drop, Geomorphology, 197, 76–84, https://doi.org/10.1016/j.geomorph.2013.04.039, 2013.

Verbovšek, T. and Gabor, L.: Morphometric properties of dolines in Matarsko podolje, SW Slovenia, Environ. Earth Sci., 78, 396, https://doi.org/10.1007/s12665-019-8398-6, 2019.

Vey, S., Al-Halbouni, D., Haghighi, M. H., Alshawaf, F., Vüllers, J., Güntner, A., Dick, G., Ramatschi, M., Teatini, P., Wickert, J., and Weber, M.: Delayed subsidence of the Dead Sea shore due to hydro-meteorological changes, Sci. Rep., 11, 13518, https://doi.org/10.1038/s41598-021-91949-y, 2021.

Virtanen, P., Gommers, R., Oliphant, T. E., Haberland, M., Reddy, T., Cournapeau, D., Burovski, E., Peterson, P., Weckesser, W., Bright, J., van der Walt, S. J., Brett, M., Wilson, J., Millman, K. J., Mayorov, N., Nelson, A. R. J., Jones, E., Kern, R., Larson, E., Carey, C. J., Polat, İ., Feng, Y., Moore, E. W., VanderPlas, J., Laxalde, D., Perktold, J., Cimrman, R., Henriksen, I., Quintero, E. A., Harris, C. R., Archibald, A. M., Ribeiro, A. H., Pedregosa, F., and van Mulbregt, P.: SciPy 1.0: fundamental algorithms for scientific computing in Python, Nat. Methods, 17, 261–272, https://doi.org/10.1038/s41592-019-0686-2, 2020.

Wadas, S. H., Tanner, D. C., Polom, U., and Krawczyk, C. M.: Structural analysis of S-wave seismics around an urban sinkhole: evidence of enhanced dissolution in a strike-slip fault zone, Nat. Hazards Earth Syst. Sci., 17, 2335–2350, https://doi.org/10.5194/nhess-17-2335-2017, 2017.

Waltham, T., Bell, F. G., and Culshaw, M. G.: Sinkholes and Subsidence: Karst and Cavernous Rocks in Engineering and Construction, Springer Science & Business Media, 405 pp., ISBN 3-540-20725-2, https://doi.org/10.1007/b138363, 2007.

Proof Only

Waskom, M. L.: seaborn: statistical data visualization, J. Open Source Softw., 6, 3021, https://doi.org/10.21105/joss.03021, 2021.

Watson, R., Bunce, C., Drew, D., Fiaschi, S., Hickey, C., Walsh, J. J., and Holohan, E.: An inception framework hypothesis for karst development in the Burren, Ireland, Geomorphology, 466, 109450, https://doi.org/10.1016/j.geomorph.2024.109450, 2024.

Watson, R. A., Holohan, E. P., Al-Halbouni, D., Saberi, L., Sawarieh, A., Closson, D., Alrshdan, H., Abou Karaki, N., Siebert, C., Walter, T. R., and Dahm, T.: Sinkholes and uvalas in evaporite karst: spatio-temporal development with links to base-level fall on the eastern shore of the Dead Sea, Solid Earth, 10, 1451–1468, https://doi.org/10.5194/se-10-1451-2019, 2019.

Yaoru, L., Feng'e, Z., Jixiang, Q., Jiaming, X., and Xiuhong, G.: Evaporite karst and resultant geohazards in China, Carbonate. Evaporite., 17, 159–165, https://doi.org/10.1007/BF03176482, 2002.

Yechieli, Y.: Fresh-Saline Ground Water Interface in the Western Dead Sea Area, Groundwater, 38, 615–623, https://doi.org/10.1111/j.1745-6584.2000.tb00253.x, 2000.

Yechieli, Y., Magaritz, M., Levy, Y., Weber, U., Kafri, U., Woelfli, W., and Bonani, G.: Late Quaternary Geological History of the Dead Sea Area, Israel, Quat. Res., 39, 59–67, https://doi.org/10.1006/qres.1993.1007, 1993.

Yechieli, Y., Abelson, M., Bein, A., Crouvi, O., and Shtivelman, V.: Sinkhole "swarms" along the Dead Sea coast: Reflection of disturbance of lake and adjacent groundwater systems, Bull. Geol. Soc. Am., 118, 1075–1087, https://doi.org/10.1130/B25880.1, 2006.

Yizhaq, H., Ish-Shalom, C., Raz, E., and Ashkenazy, Y.: Scale-free distribution of Dead Sea sinkholes: Observations and modeling, Geophys. Res. Lett., 44, 4944–4952, https://doi.org/10.1002/2017GL073655, 2017.

Proof only

Remarks from the typesetter

TS1 Please give an explanation of why this needs to be changed. We have to ask the handling editor for approval. Thanks.
TS2 Please confirm all adjusted exponential units.
TS3 Please give an explanation of why this needs to be changed. We have to ask the handling editor for approval. Thanks.
TS4 Please give an explanation of why this needs to be changed. We have to ask the handling editor for approval. Thanks.
TS5 Please give an explanation of why this needs to be changed. We have to ask the handling editor for approval. Thanks.
TS6 Please give an explanation of why this needs to be changed. We have to ask the handling editor for approval. Thanks.
TS7 Please give an explanation of why this needs to be changed. We have to ask the handling editor for approval. Thanks.
TS8 Please give an explanation of why this needs to be changed. We have to ask the handling editor for approval. Thanks.
TS9 Please give an explanation of why this needs to be changed. We have to ask the handling editor for approval. Thanks.
TS10 Please give an explanation of why this needs to be changed. We have to ask the handling editor for approval. Thanks.
TS11 Please give an explanation of why this needs to be changed. We have to ask the handling editor for approval. Thanks.
TS12 Please give an explanation of why this needs to be changed. We have to ask the handling editor for approval. Thanks.
TS13 Please give an explanation of why this needs to be changed. We have to ask the handling editor for approval. Thanks.
TS14 Please give an explanation of why this needs to be changed. We have to ask the handling editor for approval. Thanks.
TS15 Please give an explanation of why this needs to be changed. We have to ask the handling editor for approval. Thanks.
TS16 Please give an explanation of why this needs to be changed. We have to ask the handling editor for approval. Thanks.
TS17 Please give an explanation of why this needs to be changed. We have to ask the handling editor for approval. Thanks.
TS18 Please give an explanation of why this needs to be changed. We have to ask the handling editor for approval. Thanks.
TS19 Please give an explanation of why this figure needs to be changed. We have to ask the handling editor for approval. Thanks.
TS20 Please give an explanation of why the caption needs to be changed. We have to ask the handling editor for approval. Thanks.
TS21 Please give an explanation of why this figure needs to be changed. We have to ask the handling editor for approval. Thanks.
TS22 Please give an explanation of why the caption needs to be changed. We have to ask the handling editor for approval. Thanks.
TS23 Please give an explanation of why this needs to be changed. We have to ask the handling editor for approval. Thanks.
TS24 Please give an explanation of why this needs to be added. We have to ask the handling editor for approval. Thanks.
TS25 Please give an explanation of why this needs to be changed. We have to ask the handling editor for approval. Thanks.
TS26 Please give an explanation of why this needs to be changed. We have to ask the handling editor for approval. Thanks.
TS27 Please give an explanation of why this needs to be changed. We have to ask the handling editor for approval. Thanks.
TS28 Please give an explanation of why this needs to be changed. We have to ask the handling editor for approval. Thanks.
TS29 Please give an explanation of why this needs to be changed. We have to ask the handling editor for approval. Thanks.
TS30 Please give an explanation of why this needs to be changed. We have to ask the handling editor for approval. Thanks.
TS31 Please give an explanation of why this needs to be changed. We have to ask the handling editor for approval. Thanks.
TS32 Please give an explanation of why this needs to be changed. We have to ask the handling editor for approval. Thanks.
TS33 Please give an explanation of why this needs to be changed. We have to ask the handling editor for approval. Thanks.
TS34 Please give an explanation of why this needs to be changed. We have to ask the handling editor for approval. Thanks.
TS35 Please give an explanation of why this needs to be changed. We have to ask the handling editor for approval. Thanks.
TS36 Please give an explanation of why this needs to be changed. We have to ask the handling editor for approval. Thanks.
TS37 Please give an explanation of why this needs to be changed. We have to ask the handling editor for approval. Thanks.
TS38 Please give an explanation of why this needs to be changed. We have to ask the handling editor for approval. Thanks.
TS39 Please give an explanation of why this needs to be changed. We have to ask the handling editor for approval. Thanks.
TS40 Please give an explanation of why this needs to be changed. We have to ask the handling editor for approval. Thanks.
TS41 Please give an explanation of why this needs to be changed. We have to ask the handling editor for approval. Thanks.
TS42 Please give an explanation of why the unit needs to be changed. We have to ask the handling editor for approval. Thanks.
TS43 Please give an explanation of why the unit needs to be changed. We have to ask the handling editor for approval. Thanks.
TS44 Please give an explanation of why this needs to be changed. We have to ask the handling editor for approval. Thanks.
TS45 Please give an explanation of why this needs to be changed. We have to ask the handling editor for approval. Thanks.
TS46 Please give an explanation of why this needs to be changed. We have to ask the handling editor for approval. Thanks.
TS47 Please give an explanation of why this needs to be changed. We have to ask the handling editor for approval. Thanks.
TS48 Please give an explanation of why this needs to be changed. We have to ask the handling editor for approval. Thanks.
TS49 Please give an explanation of why this needs to be changed. We have to ask the handling editor for approval. Thanks.

TS50 Please give an explanation of why this needs to be changed. We have to ask the handling editor for approval. Thanks.
TS51 Please confirm DOI.
TS52 Please confirm added section and provide a text including the DOI and citation. With this section added, please check if there are any changes necessary for the data availability section.
TS53 Please confirm both Acknowledgements and Financial support sections. Please also confirm updated funding information in the MS records.
TS54 This reference is not mentioned in the text.
TS55 Please confirm DOI.

Please note the remarks at the end of the manuscript.